J. Fluid Mech. (2021), vol. 921, A11, doi:10.1017/jfm.2021.495

Large-eddy simulation on the similarity between wakes of wind turbines with different yaw angles

Zhaobin Li[1,2] **and Xiaolei Yang**[1,2,†]

[1]The State Key Laboratory of Nonlinear Mechanics, Institute of Mechanics, Chinese Academy of Sciences, Beijing 100190, PR China

[2]School of Engineering Sciences, University of Chinese Academy of Sciences, Beijing 100049, PR China

(Received 29 September 2020; revised 21 May 2021; accepted 28 May 2021)

This work is dedicated to studying the similarity between wakes of wind turbines with different yaw angles and tip speed ratios under different turbulent inflows using large-eddy simulations with actuator surface models. Simulation results show that wake characteristics from cases with different yaw angles overlap with each other when normalized properly, which include the streamwise variations of the wake deflection, the centreline velocity deficit, the widths of the wakes, the standard deviations of instantaneous wake centre positions and the instantaneous wake widths. Different scalings are proposed for the streamwise velocity deficit and the transverse velocity. The similarities observed between cases with different yaw angles and the different scalings suggest that it is proper to decompose the wake of a yawed wind turbine into a streamwise wake and a lateral wake deflection, which is critical for developing analytical models. The mean of the instantaneous wake widths and the mean of the instantaneous centreline streamwise velocity are observed as being smaller than those of the time-averaged wake. These quantities are then related by using two analytical expressions proposed in this work. The observed similarities together with the proposed analytical expressions provide a better understanding of wakes of yawed wind turbines and can be employed to develop physics-based dynamic wake models.

Key words: wakes, turbulence simulation, turbulent mixing

1. Introduction

Wind turbine wakes that feature low-wind speeds and high-turbulence intensities, which reduce the power outputs and increase the fatigue loads of downwind turbines, can significantly impact the overall performance of wind farms (Thomsen & Sørensen

---

† Email address for correspondence: xyang@imech.ac.cn

1999; Barthelmie *et al.* 2009). To mitigate the negative impacts of turbine wakes, advanced turbine control strategies have been developed and reported in the literature, e.g. axial induction factor control (Annoni *et al.* 2016), yaw-based wake control (Munters & Meyers 2018; Hoyt & Seiler 2020) and individual blade pitch control (Ossmann, Theis & Seiler 2017). Understanding how these control strategies affect the characteristics of turbine wakes is critical for their implementation in utility-scale wind farms. In this work, we focus on the wake of a yawed wind turbine, which is redirected by deliberately creating a misalignment between the rotor's axis and the inflow directions (Gebraad *et al.* 2017). Specifically, we investigate the similarity between wakes of turbines with different yaw angles for different tip speed ratios (TSR) and turbulent inflows. For a general review and perspective on the challenges in wind energy science, and recent reviews on the dynamics of wind turbine and wind farm flows, the readers can refer to the papers by Stevens & Meneveau (2017), Meneveau (2019), Veers *et al.* (2019) and Porté-Agel, Bastankhah & Shamsoddin (2020).

As a key feature of wakes of yawed turbines, the wake deflection has been extensively studied in the literature in terms of its origin and characteristics. Using hot-wire measurement in a wind tunnel of a small wind turbine with a rotor diameter $D = 0.12$ m, Medici & Alfredsson (2006) found that the wake deflection is caused by a transverse velocity, which convects the wake aside. Later, more details on the transverse velocity were revealed by Howland *et al.* (2016) using experiments on a porous disk as well as large-eddy simulation (LES) of turbines modelled using the actuator disk model and the actuator line model (ALM) under uniform inflow. Their results showed that the transverse velocity is non-uniformly distributed on the cross-section and can be described by a counter-rotating vortex pair (CVP) with vortex centres located above and below the wake centre, which not only convects the wake laterally but also deforms it into a curled shape. Moreover, the results of the ALM reveal a top-down asymmetry in the wake owing to the rotation of the rotor. Bastankhah & Porté-Agel (2016) explained the formation of the CVP based on the continuity equation. In addition, from the wind tunnel experiment of a wind turbine with $D = 0.15$ m under turbulent inflow, they confirmed the deformation and the top-down asymmetry of the wake cross-section arising from the rotor rotation as well as the tower, and named it as kidney-shape. Bartl *et al.* (2018) conducted wind tunnel measurements of a yawed-turbine model ($D = 0.90$ m) with different inflow turbulence intensities and found that the kidney-shaped deformation of the wake cross-section is largely alleviated when increasing the inflow turbulence intensity from 2 % to 10 %. Bastankhah & Porté-Agel (2016) also showed that when the yaw angle is less than 30°, as in real-world applications, the kidney-shaped deformation may not be significant, so the wake cross-section can be approximated by an ellipse with a horizontal minor axis.

To facilitate the design and operation of wind farms, analytical models have been derived in the literature for fast prediction of wakes of yawed turbines. An important aim of these models is to predict the wake deflection. In the model of Jiménez, Crespo & Migoya (2010), the far wake's transverse velocity for computing the wake deflection is related to the lateral component of the thrust on the rotor based on the momentum theory. Later, it was found that this model may overpredict the wake deflection (Jiménez *et al.* 2010; Shapiro, Gayme & Meneveau 2018). To solve this problem, Shapiro *et al.* (2018) proposed a model based on the analogy of a yawed wind turbine to a finite elliptical wing. In the proposed model, the transverse velocity in the wake is assumed to be equal to the the downwash on the wing created by the CVP according to Prantl's lifting line theory. Shapiro's model predicts, in general, a smaller wake deflection compared with that of Jiménez *et al.* (2010). A validation of the model of Shapiro *et al.* was carried out using the simulation results of an actuator disk model and the wind tunnel measurements of Bastankhah & Porté-Agel (2016). It was found that the key to successfully predicting the wake deflection is to accurately compute the transverse velocity, which gradually decreases with the downstream distance to the turbine. Both the models of Jiménez *et al.* and Shapiro *et al.* attribute the gradual decrease of lateral velocity to the wake expansion, and assume that the wake widths defined by the streamwise velocity and the transverse velocity are equal, so that the wake width computed from the streamwise velocity can be employed for the transverse velocity. The above assumption is also adopted by other analytical wake models, e.g. by Bastankhah & Porté-Agel (2016) and Qian & Ishihara (2018). However, this assumption has not yet been proven and may introduce errors, as pointed out by Jiménez *et al.* (2010). To this end, a part of this work will be dedicated to verifying if the wake widths defined by the velocity in the streamwise and spanwise directions are equal. Once the wake centreline is known along the streamwise direction, the model for the time-averaged velocity deficit can be developed based on the self-similarity. The self-similarity means that the velocity deficit profiles in the far wake can be fitted to a Gaussian function and they overlap with each other if the deficit is normalized by its local maximum and the abscissas are normalized by the wake width (Wu & Porté-Agel 2012; Zhang, Markfort & Porté-Agel 2013; Chamorro *et al.* 2015; Fuertes, Markfort & Porté-Agel 2018). For non-yawed turbines, Bastankhah & Porté-Agel (2014) developed an analytical wake model with Gaussian wake profiles assuming axisymmetry and self-similarity. Later, by assuming the elliptical cross-section shape, Abkar & Porté-Agel (2015) extended this model to take into account the different lateral and vertical growth rates, which are caused by the inflow shear and ground effects (Xie & Archer 2015). Bastankhah & Porté-Agel (2016) explored the self-similarity of the wake behind a yawed wind turbine and found that the velocity deficit in the horizontal plane can still be fitted accurately to Gaussian functions with respect to the wake centre and proposed an analytical wake model for yawed wind turbines to predict the time-averaged velocity deficit.

With the aforementioned models, the wake deflection can be predicted with reasonable accuracy. However, to realize yaw-based wake steering for the optimal wind farm design and operation, fast analytical models need to be developed to predict more features of the wake of a yawed wind turbine, which include both the time-averaged quantities (e.g. the wake width and the time-averaged velocity deficit) and the instantaneous quantities (e.g. the instantaneous wake influencing region). Most of the existing analytical models for wakes of yawed turbines have been focused on the deflection and velocity deficit of the time-averaged wake. For instance, the analytical wake model of Bastankhah & Porté-Agel (2016), which was developed based on the self-similarity of the streamwise velocity and the skew angle observed in the far wake, can predict the time-averaged velocity distribution and wake deflection of yawed wind turbines. On the other hand, high-fidelity models, e.g. LES with actuator surface/line models for turbine blades, can accurately predict various additional aspects of the wake. However, it is still not feasible to use high-fidelity models for the optimization of wind farm design and operations owing to the expensive computational cost and the large number of cases to be simulated in an optimization process. Meanwhile, similarities of turbine wakes have been observed from the LES results for different wind turbine designs (Foti, Yang & Sotiropoulos 2018), different inflow (Yang *et al.* 2015*a*) and different turbine operational conditions (Yang & Sotiropoulos 2019*b*). Yang *et al.* (2015*a*) and Foti *et al.* (2018) found that the turbine-added turbulence kinetic energies overlap with each other when normalized using a velocity scale defined by the thrust on the rotor for different inflows and turbine designs. Moreover, similarities are observed for the statistics of the meandering motion of the wake when normalized using a velocity scale based on the thrust on the rotor for the meandering, owing to bluff body shear layer instability (Foti *et al.* 2018), and the diameter D for the meandering, owing to large eddies in the incoming turbulent flow (Yang & Sotiropoulos 2019*b*). If the similarity also exists in turbine wakes for different yaw angles, then there is a potential that fast models can be derived for predicting various aspects of wakes for yawed turbines based on such a similarity and several typical high-fidelity simulations. However, it should be noted that having similarities, especially for the present work (where only one turbine is considered), is just one step towards the development of advanced models based on physics and data from simulations and measurements. High-fidelity simulations provide a way to improve our understanding on wake dynamics but under relatively simple wind conditions. In real-life applications, computationally efficient models for heterogeneous wind conditions, wind farm layouts, complex terrains and others are needed, which can be developed by leveraging the power of low-fidelity models, e.g. the boundary-layer equation (Ainslie 1988) and machine learning methods (Duraisamy, Iaccarino & Xiao 2019; Brunton, Noack & Koumoutsakos 2020).

The objective of this work is to examine the similarity between turbines with different yaw angles with regards to the wake deflection and the wake on the frame of reference fixed on the deflected wake centre. It is noted that the similarity we discuss in this work is different from the self-similarity of turbine wakes reported in the literature. The self-similarity does not necessarily guarantee the similarity between wakes of turbines with different yaw angles. Investigation on such a similarity will provide a way to evaluate a fundamental assumption for developing analytical models, e.g. the works of Bastankhah & Porté-Agel (2016) and Shapiro *et al.* (2018), where the wake of a yawed wind turbine can be decomposed into the streamwise turbine wake and the lateral wake deflection. Specifically, we conduct a series of simulations of the EOLOS wind turbine (Hong *et al.* 2014; Chamorro *et al.* 2015) at four different yaw angles (i.e. $\gamma = 0^\circ, 10^\circ, 20^\circ, 30^\circ$) for different TSRs under different turbulent inflows. The wind turbine wake is simulated using LES with the wind turbine's blades and nacelle modelled as actuator surfaces (Yang & Sotiropoulos 2018). The time-averaged velocity field, turbine-added Reynolds stress, and the instantaneous wake positions and widths are systematically examined. Different scaling factors are derived to describe the similarity of these wake characteristics. Two analytical expressions are also proposed to relate the instantaneous wake width and velocity deficit with their time-averaged counterparts.

The rest of the paper is structured as follows. In § 2, we describe the employed numerical methods and the simulation set-up. Then in §§ 3–5, we present the results on the similarity of the time-averaged wake velocity field and statistics of the wake turbulence for different turbine operation conditions and turbulent inflows. Finally, we summarize the findings from this work and draw conclusions in § 6.

2. Numerical methods and simulation set-up

2.1. *Flow solver*

The turbulent flow was solved using the LES module of the Virtual Flow Simulator code (VFS-Wind). The capability of the employed code for simulating turbine wakes has been extensively validated using wind tunnel (Yang *et al.* 2015*b*) and field measurements (Yang, Pakula & Sotiropoulos 2018; Yang *et al.* 2021). The code is open source and available at GitHub. (https://github.com/SAFL-CFD-Lab/VFS-Wind.) The governing equations are the filtered incompressible Navier–Stokes equations in curvilinear coordinates shown as

$$J\frac{\partial U^i}{\partial \xi^i} = 0, \tag{2.1}$$

$$\frac{1}{J}\frac{\partial U^i}{\partial t} = \frac{\xi_l^i}{J}\left(-\frac{\partial}{\partial \xi^j}\left(U^j u_l\right) + \frac{\mu}{\rho}\frac{\partial}{\partial \xi^j}\left(\frac{g^{jk}}{J}\frac{\partial u_l}{\partial \xi^k}\right) - \frac{1}{\rho}\frac{\partial}{\partial \xi^j}\left(\frac{\xi_l^j p}{J}\right) - \frac{1}{\rho}\frac{\partial \tau_{lj}}{\partial \xi^j} + f_l\right), \tag{2.2}$$

where $i, j, k, l = \{1, 2, 3\}$ are the tensor indices and ξ^i are the curvilinear coordinates related to the Cartesian coordinates x_l by the transformation metrics $\xi_l^i = \partial\xi^i/\partial x_l$. Additionally, J denotes the Jacobian of the geometric transformation, $U^i = (\xi_l^i/J)u_l$ is the contravariant volume flux with u_l as the velocity in Cartesian coordinates, μ denotes the dynamic viscosity, ρ is the fluid density, $g^{jk} = \xi_l^j\xi_l^k$ are the components of the contravariant metric tensor, p is the pressure and f_l are body forces introduced by the actuator-type wind turbine model. In the momentum equation, τ_{ij} is the subgrid-scale (SGS) stress, which is computed using the dynamic Smagorinsky model (Smagorinsky 1963; Germano *et al.* 1991). The governing equations are discretized on a structured curvilinear grid. A second-order accurate central differencing scheme is used for the spatial discretization with a second-order fractional step method (Ge & Sotiropoulos 2007) for the temporal integration. The momentum equation is solved with the matrix-free Newton–Krylov method (Knoll & Keyes 2004). The pressure Poisson equation, for satisfying the continuity constraint, is solved using the generalized minimal residual (GMRES) method with an algebraic multi-grid acceleration (Saad 1993).

2.2. *Wind turbine parametrization method*

Geometry-resolving simulations of wind turbine wakes are extremely expensive, because the characteristic length of wind turbine wakes is often more than two orders of magnitude larger than the thickness of the boundary layer over the blades. (The length scale of wind turbine wakes is proportional to the rotor's diameter D; the thickness of the boundary layer on the blade is approximately 1 cm for a turbine of $D \approx 100$ m operating in region II, i.e. when the wind velocity is between the cut-in and the rated speeds Yang & Sotiropoulos 2018) For this reason, the aerodynamics of wind turbines is often parametrized using actuator disk (Chattot 2014), actuator line (Sorensen & Shen 2002) or actuator surface (Shen, Zhang & Sorensen 2009; Yang & Sotiropoulos 2018) models. In this work, the class of well validated actuator surface (AS) models for turbine blades and nacelle proposed by Yang & Sotiropoulos (2018) was employed. The AS model represents each rotor blade with a simplified two-dimensional (2-D) surface defined by the chord length and the twist angle at each radial location. The lift and drag forces $\boldsymbol{L}$ and $\boldsymbol{D}$ at each radial location were determined using the tabulated airfoil data using the local instantaneous relative incoming velocity as follows:

$$\boldsymbol{L} = \tfrac{1}{2}\rho C_L c|V_{ref}|^2\boldsymbol{e_L} \tag{2.3}$$

and

$$\boldsymbol{D} = \tfrac{1}{2}\rho C_D c|V_{ref}|^2\boldsymbol{e_D}, \tag{2.4}$$

where c is the chord length, V_{ref} is the instantaneous incoming velocity relative to the rotating blade at the computing point averaged over the chord length, $\boldsymbol{e}_L$ and $\boldsymbol{e}_D$ are the

	Inflow 1	Inflow 2	Inflow 3
$\gamma = 0^\circ$	$\tilde{\lambda} = \{7, 8, 9\}$	$\tilde{\lambda} = 8$	$\tilde{\lambda} = 8$
$\gamma = 10^\circ$	$\tilde{\lambda} = \{7, 8, 9\}$	$\tilde{\lambda} = 8$	$\tilde{\lambda} = 8$
$\gamma = 20^\circ$	$\tilde{\lambda} = \{7, 8, 9\}$	$\tilde{\lambda} = 8$	$\tilde{\lambda} = 8$
$\gamma = 30^\circ$	$\tilde{\lambda} = \{7, 8, 9\}$	$\tilde{\lambda} = 8$	$\tilde{\lambda} = 8$
Pure inflow	No turbine	No turbine	No turbine

Table 1. Summary of simulation cases: γ denotes the yaw angle, $\tilde{\lambda}$ denotes the TSR defined with the inflow velocity projected along the rotor's axis.

unit directional vectors of the lift and drag forces, and C_L and C_D are the lift and the drag coefficients defined in 2-D airfoil tables as a function of Reynolds number and the angle of attack. Corrections including the three-dimensional stall delay model (Du & Selig 1998) and the tip loss correction (Shen *et al.* 2005) were applied. With the computed $\boldsymbol{L}$ and $\boldsymbol{D}$, the body force in (2.2) was calculated by uniformly distributing the forces along the chord as follows:

$$\boldsymbol{f} = (\boldsymbol{L} + \boldsymbol{D})/c. \tag{2.5}$$

A smoothed discrete delta function (Yang *et al.* 2009) was employed for transferring quantities between the actuator surface and the background grid nodes for solving the flow.

2.3. *Simulation set-up*

In this section, we present the set-up of the cases simulated in this work, as summarized in table 1. Four different yaw angles γ, i.e. $\gamma = 0^\circ, 10^\circ, 20^\circ, 30^\circ$ (one extra case of $\gamma = -30^\circ$ was also conducted to check the influence of negative yaw angle in Appendix D.), defined as the misalignment between the inflow and the rotor axis (shown in figure 1), were considered for three turbulent inflows with different levels of turbulence intensity. For inflow 1, the effects of different turbine operation conditions (tip speed ratios) were examined for different fixed yaw angles. For inflows 2 and 3, simulations were conducted under the same turbine operating conditions to investigate the influence of the inflow turbulence on the wake. For each inflow, an extra case without the wind turbine was also simulated to provide the reference turbulent boundary layer flow. All the simulations were conducted with the same set-up, i.e. the same boundary and initial conditions, and the same time step to ensure the inflow turbulent structures were synchronized for the simulated cases to facilitate the one-to-one comparison of instantaneous flow fields. Details on the employed wind turbine, the computational domain and the boundary conditions, and the turbulent inflow generation are provided in the following subsections.

2.3.1. *Wind turbine and operation conditions*

We simulated the three-blade horizontal-axis Clipper Liberty 2.5 MW wind turbine located at the EOLOS wind energy research field station at the University of Minnesota, USA. The rotor diameter was $D = 96$ m, the hub was at $z_{hub} = 80$ m, and the nacelle had a cuboid-like shape with its dimensions being approximately equal to $5.3\ \text{m} \times 4.7\ \text{m} \times 5.5$ m. The tower was conical with diameters varying from 3.0 m at the top to 4.1 m at the bottom. It should be noted that the tower was not modelled in this work, which may affect

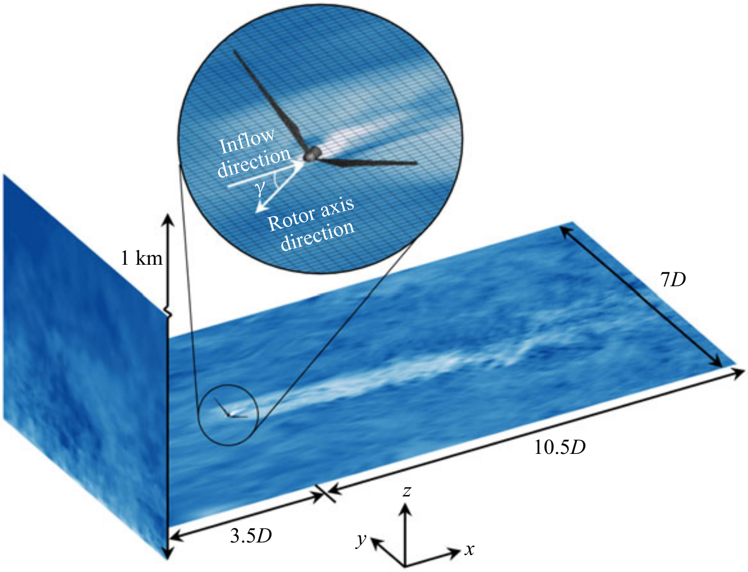

Figure 1. Schematic of the computational set-up employed for simulating the wake of a yawed wind turbine.

the top-down asymmetry of the wake of a yawed wind turbine as reported by Howland *et al.* (2016). More information about the EOLOS wind turbine can be found in the papers by Hong *et al.* (2014) and Chamorro *et al.* (2015).

In each simulation, the rotor rotated at a fixed modified TSR with respect to the project velocity U_d normal to the rotor sweeping plane, as follows:

$$\tilde{\lambda} = \frac{\varOmega R}{U_d}, \tag{2.6}$$

where $\varOmega$ is the angular velocity of the rotor, $R = 48$ m is the radius of the rotor and

$$U_d = U_\infty \cos\gamma \tag{2.7}$$

is the inflow velocity projected in the rotor's axis direction.

The scenario we study herein is ideal, where the rotor rotates based on the modified TSR $\tilde{\lambda}$, which cannot be easily realized in real-life applications. Defining the TSR based on the velocity projected to the axial direction of the rotor was for the convenience of explaining how we control the rotational speed of the rotor in this work. It does not guarantee optimal energy conversion of a yawed wind turbine (Bastankhah & Porté-Agel 2019). Three different modified TSRs $\tilde{\lambda} = \{7, 8, 9\}$ were employed to vary the thrust and power coefficients to investigate the effects of operation conditions on wake characteristics of yawed wind turbines.

2.3.2. *Computational domain and boundary conditions*

We employed the same computational domain for all the cases, which is shown in figure 1. The size of the computational domain was $L_x \times L_y \times L_z = 14D \times 7D \times 1$ km in the streamwise (x), transverse (y) and vertical (z) directions, respectively. The origin of the coordinates coincided with the wind turbine's footprint on the ground. The domain was discretized by a Cartesian grid with grid nodes of $N_x \times N_y \times N_z = 281 \times 281 \times 143$.

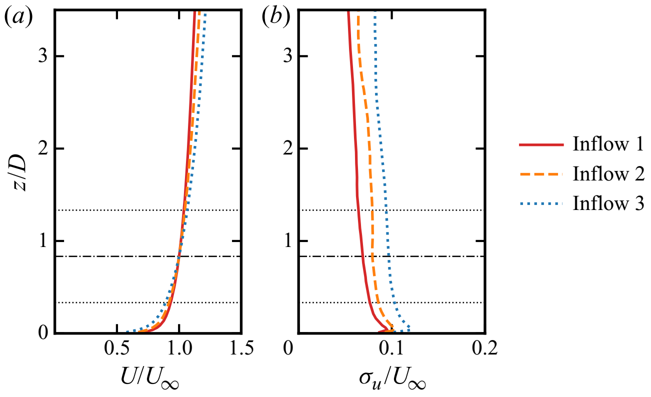

Figure 2. Characteristics of the turbulent inflows: (*a*) the time-averaged streamwise velocity profile; and (*b*) the streamwise turbulence intensity profile. The turbulence intensity at hub height for inflows 1, 2 and 3 are 6.9 %, 7.9 % and 9.6 %, respectively. The horizontal dash–dotted lines represent the turbine hub height and the dotted lines represent the upper and the lower limits of the rotor.

The grid was uniform in the x, y directions with the grid spacing $\Delta x = D/20$ and $\Delta y = D/40$. In the z direction, the grid was uniform near the ground ($z \in (0, 2D)$) with $\Delta z = D/40$ and was gradually stretched to the top boundary. A grid independent study is presented in Appendix C. Turbulent inflows generated by a precursory simulation (to be explained in the next section) were prescribed at the inlet ($x = -3.5D$). At the outlet ($x = 10.5D$), the Neumann boundary condition for velocity (i.e. $\partial u_i/\partial x = 0$) was applied. A wall model based on the logarithmic law for rough walls was applied on the ground, i.e. $u/u^* = (1/\kappa)\ln(z/z_0)$, where u^* is the friction velocity, κ is the Kármán constant and z_0 is the roughness length (Blocken, Stathopoulos & Carmeliet 2007). The roughness length was set according to the inflow conditions. At the lateral and the top boundaries, the free-slip condition was applied. The time step was $0.018D/U_\infty$. All simulations were first run for approximately 40 rotor revolutions to achieve a fully developed state. Then the simulations were continued for another approximately 600 rotor revolutions (corresponding to 45 minutes in physical time) for computing the statistics of the wake. The total number of rotor revolutions was computed based on the rotor rotational speed of the $\tilde{\lambda} = 8$ and $\gamma = 0^\circ$ case.

2.3.3. *Turbulent inflow*

The turbulent inflows were generated from precursory LESs with a larger computational domain ($L_x^{'} \times L_y^{'} \times L_z^{'} = 62D \times 46D \times 1$ km) to capture large-scale eddies in the atmospheric boundary layer (Wang & Zheng 2016; Liu, Wang & Zheng 2019). Periodic boundary conditions were applied in the horizontal directions. The top boundary was set as free-slip. The lower boundary was set as no-slip and modelled using the logarithmic law for rough walls, as in the turbine simulations. Three different ground roughness lengths were considered, i.e. $z_0 = 0.00016$ m, 0.001 m, 0.01 m for inflow 1, inflow 2 and inflow 3, respectively. The characteristics of the inflows are shown in figure 2. In the precursory simulations, the velocity fields on a $y-z$ plane were saved at each time step and then applied at the inlet of the turbine simulations. Linear interpolations were carried out if necessary.

$\tilde{\lambda}$	7	8	9
$\tilde{C}_T$	0.654	0.710	0.711
$\tilde{C}_P$	0.443	0.488	0.487

Table 2. Modified thrust and power coefficients at different modified TSRs.

3. Similarity of time-averaged wake characteristics

In this section, we present the wake characteristics of the time-averaged velocity field for different yaw angles under different turbine operation conditions with inflow 1. The wake characteristics to be examined include the wake centreline deflection, the streamwise velocity deficit, the yaw-induced transverse velocity, and the wake widths defined by the streamwise velocity deficit and transverse velocity. We examined different scaling factors for different wake characteristics. It is noted that some of the scaling factors can be found in the literature (Jiménez *et al.* 2010; Bastankhah & Porté-Agel 2016; Shapiro *et al.* 2018), and the derivations of the employed scaling factors are shown in Appendix A.

3.1. *Variation of the thrust and power with yaw angles*

Before probing into the flow fields, the variations of the computed thrust (normal to the rotor sweep plane) and power (calculated from the shaft torque) with yaw angles are compared in figure 3. The results were normalized by the value at $\gamma = 0^\circ$ at each corresponding modified TSR $\tilde{\lambda}$. All results agreed well with the prediction obtained using the axial momentum theory (Burton *et al.* 2011), which states that the thrust T and power P scale with $\cos^2(\gamma)$ and $\cos^3(\gamma)$, respectively. This relation has also been observed in other numerical and experimental studies (Krogstad & Adaramola 2012; Bartl *et al.* 2018). With this relation, the thrust and power coefficients ($\tilde{C}_T$ and $\tilde{C}_P$), which are defined with respect to U_d and shown as

$$\tilde{C}_T = \frac{T}{\frac{1}{2}\rho A U_d^2} = \frac{T}{\frac{1}{2}\rho A \left(U_\infty \cos\gamma\right)^2}, \tag{3.1}$$

$$\tilde{C}_P = \frac{P}{\frac{1}{2}\rho A U_d^3} = \frac{P}{\frac{1}{2}\rho A \left(U_\infty \cos\gamma\right)^3}, \tag{3.2}$$

are independent of the yaw angles and are equal to those in the non-yawed cases, because of $T \propto \cos\gamma^2$ and $P \propto \cos\gamma^3$. The values of $\tilde{C}_T$ and $\tilde{C}_P$ for different TSR are shown in table 2. It is worth noting that the yaw angle independence of $\tilde{C}_T$ and $\tilde{C}_P$ may result from the control strategy employed in the present work, i.e. the modified TSR $\tilde{\lambda}$ was fixed. However, if another control strategy is employed, the thrust T and the power P may follow $\cos^a\gamma$ and $\cos^b\gamma$, respectively, with $a < 2$ and $b < 3$ (Bastankhah & Porté-Agel 2019; Howland *et al.* 2020; Liew, Urbán & Andersen 2020). Making the comparison in figure 3 is just to verify the implementation of this idealized rotor control rather than indicating that the power and thrust should vary in that way in real-life applications.

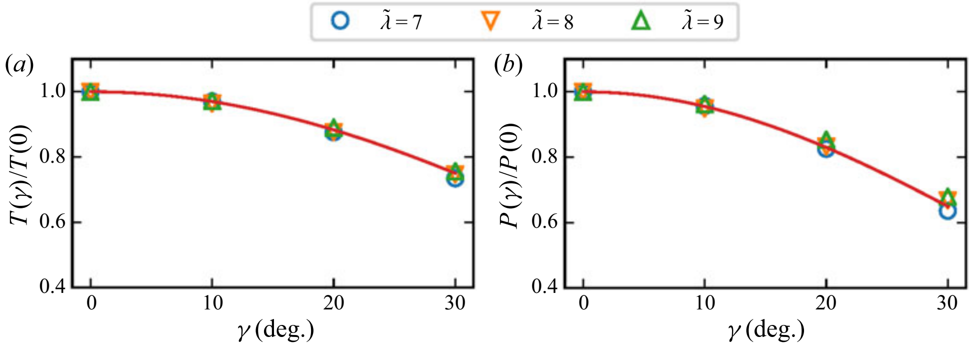

Figure 3. Influence of yaw angle γ on the rotor's thrust and power: (*a*) the normalized thrust $T(\gamma)/T(0)$ (symbols) compared with $\cos^2\gamma$ (solid line); and (*b*) the normalized power $P(\gamma)/P(0)$ (symbols) compared with $\cos^3\gamma$ (solid line). Here, $T(0)$ and $P(0)$ are the thrust and the power at $\gamma = 0$, respectively.

3.2. *Time-averaged velocity fields*

In this subsection, we examine the influence of yaw angle on the time-averaged wake velocity. To illustrate such an influence, we first plot, in figure 4, the streamwise and the transverse velocities U and V on the hub-height plane for cases with $\tilde{\lambda} = 8$ (the cases with other $\tilde{\lambda}$ have a similar pattern). The red thick dashed lines and the red dotted lines plot the wake centreline ($y = Y_C(x)$) and the boundary ($y = Y_C(x) \pm R_{1/2}(x)$) obtained by fitting the time-averaged velocity deficit using the Gaussian fit at each downstream location (x), as follows,

$$\Delta U(x, y) = U_\infty - U(x, y) = \Delta U_C(x) \exp\left(-\frac{(y - Y_C(x))^2}{2S^2(x)}\right), \tag{3.3}$$

where $U(x, y)$ is the streamwise velocity and $S(x)$ is the standard deviation of the Gaussian distribution to be fitted with the velocity profile. A schematic of these definitions is illustrated in figure 5. The wake half-width is defined as $R_{1/2}(x) = \sqrt{2\ln 2}S(x)$, which gives the distance from $Y_C(x)$ to the position where $\Delta U = (\Delta U_C)/2$.

First, figure 4 shows that the streamwise velocity U behaves similarly in the yawed and non-yawed cases. As seen, U is symmetric with respect to the wake centreline. The overall patterns of U computed at different yaw angles are very similar, although the magnitude of the velocity deficit (ΔU) and the wake width ($R_{1/2}$) gradually reduce with the increase of yaw angle owing to the reduction of the streamwise thrust on the rotor $T_x = T\cos\gamma$ and the projected rotor width $\tilde{R} = R\cos\gamma$.

In contrast, the transverse velocity V behaves differently in yawed and non-yawed cases, as seen in the second column of figure 4. In the region close to the rotor, a diverging transverse velocity is observed for all yaw angles, which is related to the expansion of the streamtube at the rotor. In this region, it is difficult to distinguish the yaw-induced transverse velocity and that induced by the wake expansion. Differences are observed in the far wake: in the non-yawed case, the transverse velocity is close to zero and is symmetrical to the wake centreline; when the rotor yaws, on the other hand, a transverse velocity in the negative y direction is observed and its magnitude increases with yaw angle. More importantly, the transverse velocity is observed as being asymmetric with respect to the wake centreline $Y_C(x)$ defined by the streamwise velocity deficit. That the transverse velocity resides only on one side of the wake centreline (behind the leading

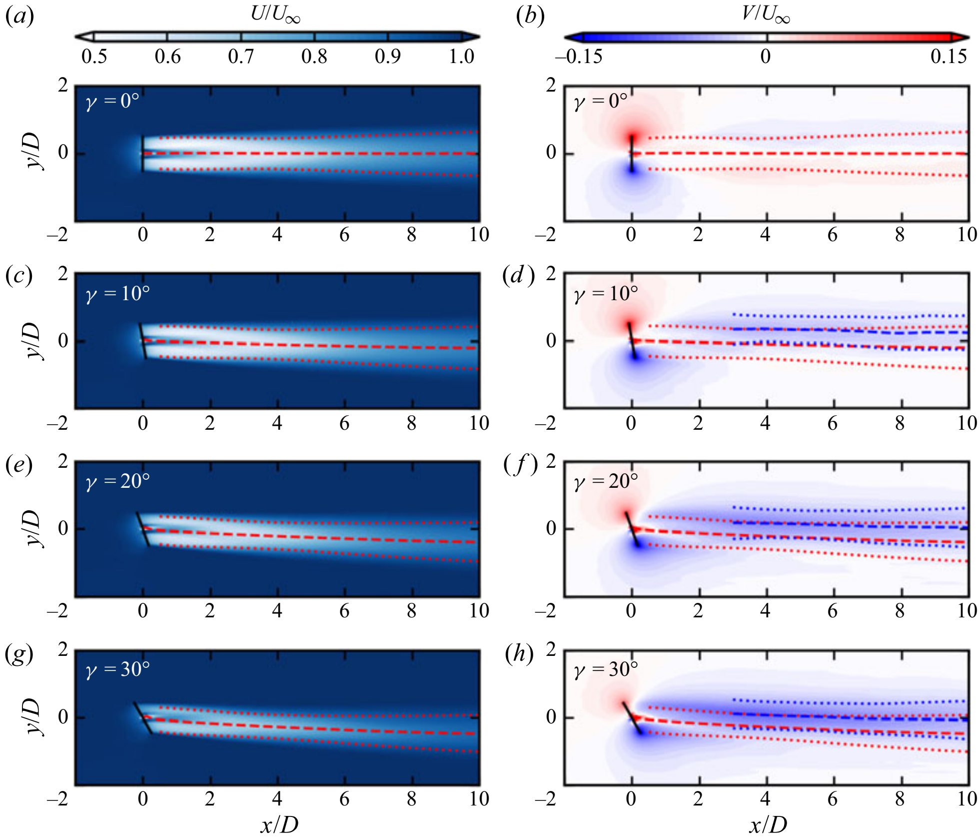

Figure 4. The time-averaged velocity field behind wind turbines (at hub-height plane $z = z_{hub}$): (*a*,*c*,*e*,*g*) streamwise velocity; and (*b*,*d*,*f*,*h*) the transverse velocity. Panels in each column are ordered by increasing yaw angle . The red dashed lines represent the centrelines of the streamwise velocity deficit. The red dots denote the wake width where the streamwise velocity deficit is half that on the centreline. The blue dashed line and blue dots denote the wake centreline and width defined by the transverse velocity. The black solid lines illustrate the rotors.

edge of the yawed rotor) is in agreement with the wind tunnel measurement of Bastankhah & Porté-Agel (2016). Owing to these differences observed in the transverse velocity V as compared with the streamwise velocity U, it is expected that the wake quantities defined by U and V should be treated differently. For this reason, we plot in addition the wake centre position $Y_C^V(x)$ and the wake width of $R_{1/2}^V(x)$, where the transverse velocity V is reduced to half of the maximum. As seen, $Y_C^V(x)$ (the blue dash lines) approximately overlaps with the streamwise wake boundary (the red dots).

In the following subsections, we will examine the similarity of these wake characteristics, using the different characteristic length and velocity scales presented in Appendix A.

3.3. *Similarity of wake centreline* $Y_C(x)$

In figure 6, we examine the similarity of the wake centreline $Y_C(x)$ for different yaw angles. The length scale employed to normalize $Y_C(x)$ is

$$Y_N = D\tilde{C}_T \cos^2 \gamma \sin \gamma, \tag{3.4}$$

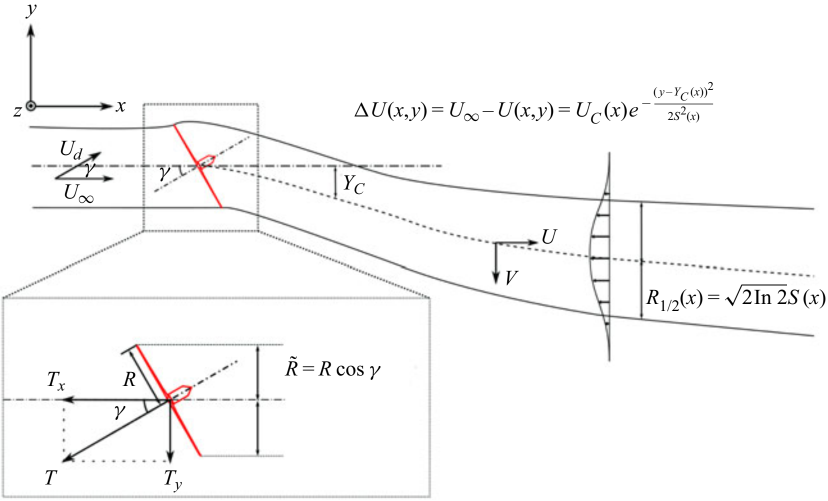

Figure 5. Schematic and and key variables for describing the wake behind a yawed wind turbine on the hub-height plane, where U_∞ is the inflow velocity, U_d is the inflow velocity component in the rotor's axis direction, γ is the yaw angle, T is the thrust on the rotor and $R = 0.5D$ is the rotor's radius. Here, U and V denote the streamwise and the transverse velocity, respectively.

which is proportional to the transverse thrust T_y as shown by Jiménez *et al.* (2010) and Shapiro *et al.* (2018). Figure 6(*a*) shows that the wake centreline deflections increased with yaw angle. For the same yaw angle, it was observed that $Y_C(x)$ increases with $\tilde{\lambda}$ at the far wake especially for the $\gamma = 30^\circ$ case. However, the differences of Y_C between cases of different $\tilde{\lambda}$ are small because of the relative small difference in the thrust coefficients C_T. In figure 6(*b*), it is observed that the wake centrelines of different yaw angles overlap with each other after being normalized by Y_N. This good scaling shows that the length scale ((3.4)) well describes the similarity of the wake centreline despite the complex dynamics of yawed turbine wakes. Once the wake centreline is known for one yaw angle, it can be generalized with the proposed length scale Y_N to predict the wake centrelines at other yaw angles if the similarity observed in this work also exists in realistic conditions taking into account the effects of thermal stability, wind speed shear, wind direction, wake interaction, etc.

3.4. *Similarity of streamwise velocity deficit* ΔU

In this section, we examine the similarity of the quantities related to the streamwise velocity deficit. The characteristic velocity employed for scaling is

$$U_N = U_\infty \left(1 - \sqrt{1 - \tilde{C}_T \cos^2 \gamma}\right), \tag{3.5}$$

which represents the streamwise velocity reduction caused by the rotor (Burton *et al.* 2011; Bastankhah & Porté-Agel 2016; Shapiro *et al.* 2018). In figure 7, we first examine the streamwise evolution of the velocity deficits $\Delta U_C(x)$ along the wake centreline for different yaw angles and different $\tilde{\lambda}$. Figure 7(*a*) shows that $\Delta U_C(x)$ with different $\tilde{\lambda}$ and different yaw angles deviates from each other, which reveals the influence of both factors. For the same $\tilde{\lambda}$, $\Delta U_C(x)$ decreases with the increase of yaw angle. For the same yaw angle,

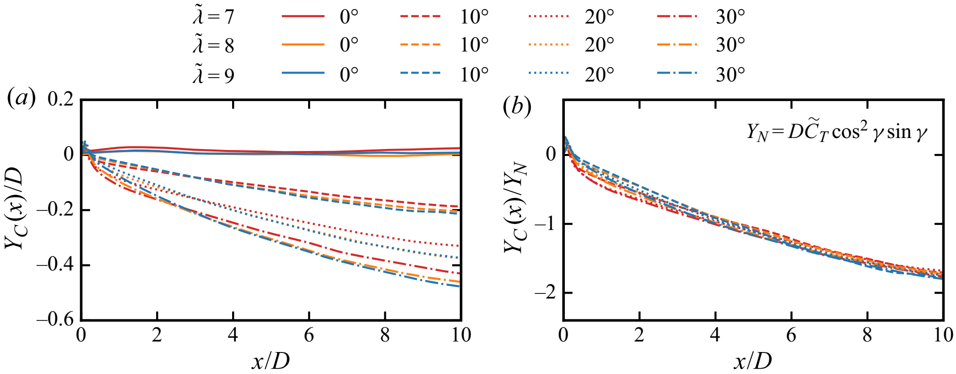

Figure 6. Wake centreline $Y_C(x)$: (*a*) normalized by the rotor's diameter D; and (*b*) normalized by the length scale $Y_N = D\tilde{C}_T \cos^2\gamma \sin\gamma$.

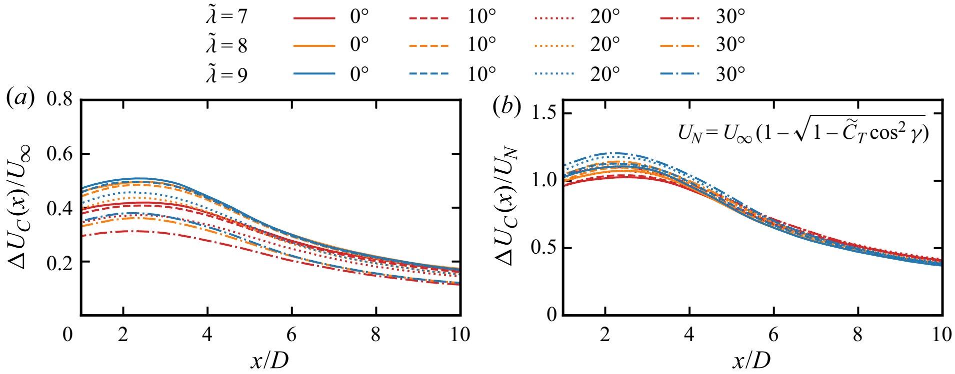

Figure 7. The characteristic velocity deficit $\Delta U_C(x)$ for different $\tilde{\lambda}$ and yaw angles: (*a*) normalized by the inflow velocity U_∞; and (*b*) normalized by the velocity scale as $U_N = U_\infty(1 - \sqrt{1 - \tilde{C}_T \cos^2\gamma})$.

$\Delta U_C(x)$ increases when increasing $\tilde{\lambda}$ owing to the increase of $\tilde{C}_T$. More importantly, at all considered downstream locations ($1D \le x \le 10D$), the $\Delta U_C(x)$ profiles are observed to vary in a similar manner. This similarity is further confirmed in figure 7(*b*), which shows the $\Delta U_C(x)$ profiles overlap with each other when normalized using the characteristic velocity U_N. In the figure, it is also noticed that $\Delta U_C(x)$ first increases until approximately $x = 2.5D$ and then gradually decreases to far-wake locations. This flow deceleration is related to the recovery of the pressure. In the far wake, the scaled wake centre velocities $\Delta U_C(x)/U_N$ show an excellent agreement with each other, which indicates U_N is the proper velocity scale for the velocity deficit.

We then examined the wake half-width $R_{1/2}(x) = \sqrt{2\ln 2}S(x)$, where $S(x)$ is obtained by fitting the velocity deficit to the Gaussian function ((3.3)). The initial wake width R_N, derived using the streamwise one-dimensional momentum theory (details can be found in Appendix A), was employed for the normalization. The expression of R_N is shown

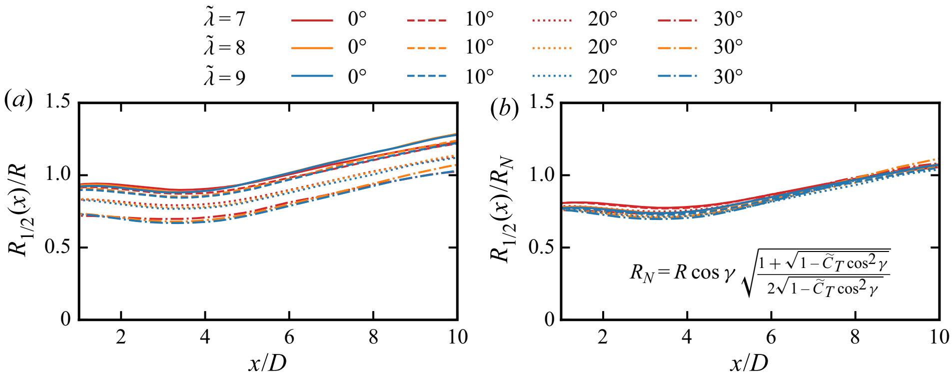

Figure 8. The characteristic wake width $R_{1/2}(x)$ for different $\tilde{\lambda}$ and yaw angles: (*a*) normalized by the rotor radius R; and (*b*) normalized by the length scale $R_N = R\cos\gamma\sqrt{(1+\sqrt{1-\tilde{C}_T\cos^2\gamma})/(2\sqrt{1-\tilde{C}_T\cos^2\gamma})}$.

as follows:

$$R_N = R\cos\gamma\sqrt{\frac{1+\sqrt{1-\tilde{C}_T\cos^2\gamma}}{2\sqrt{1-\tilde{C}_T\cos^2\gamma}}}, \tag{3.6}$$

which is a function of the thrust coefficient $\tilde{C}_T$, yaw angle γ and the rotor's radius R. Figure 8(*a*) shows that there were differences in $R_{1/2}/R$ for the cases with different yaw angles and different $\tilde{\lambda}$, but the curves overlapped when normalizing $R_{1/2}$ using R_N, as shown in figure 8(*b*). That the curves overlap with each other at all considered downstream locations in the range of $1D < x < 10D$ shows that the proposed length scale R_N, a characteristic wake width scale in the near wake, is still valid in the far wake. It is also noticed that the wake width decreased slightly in the initial near-wake region, which was attributed to the difficulties in fitting the velocity deficit profiles to the Gaussian function when the root loss phenomenon is present, as shown in figure 4. It is noted that R_N is different from that in the paper by Bastankhah & Porté-Agel (2016) for predicting the wake width at the onset of far wake (see details in Appendix B).

In figure 9, the similarity of the horizontal profiles of the streamwise velocity deficit at different turbine downstream locations is examined. Figure 9(*a*–*d*) shows the magnitude of the velocity deficit and the wake width decrease when increasing the yaw angles. In contrast, the transverse profiles of the streamwise velocity deficit shown in figure 9(*e*–*h*) overlap with each other when normalized using the velocity scale U_N and the length scale R_N, and are shifted with respect to the wake centreline $Y_C(x)$. It is seen from figure 9(*e*–*h*) that the velocity deficit profiles are symmetrical to the wake centreline for different yaw angles including $\gamma = 30^\circ$. The characteristic wake width scale R_N and velocity deficit scale U_N are proper for describing the similarity of velocity deficits for different yaw angles. It is noticed that at $3D$ turbine downstream, the velocity deficits $\Delta U/U_N$ on the plateau are approximately equal to 1, which indicates that the present scaling factor U_N is a good estimation of the velocity deficit in the near wake. Furthermore, the overlapping of the velocity deficit profiles at further turbine downstream locations (figure 9*f*–*h*) shows that U_N successfully describes the similarity of the velocity deficits for different yaw angles, although it is derived at the imminent near wake.

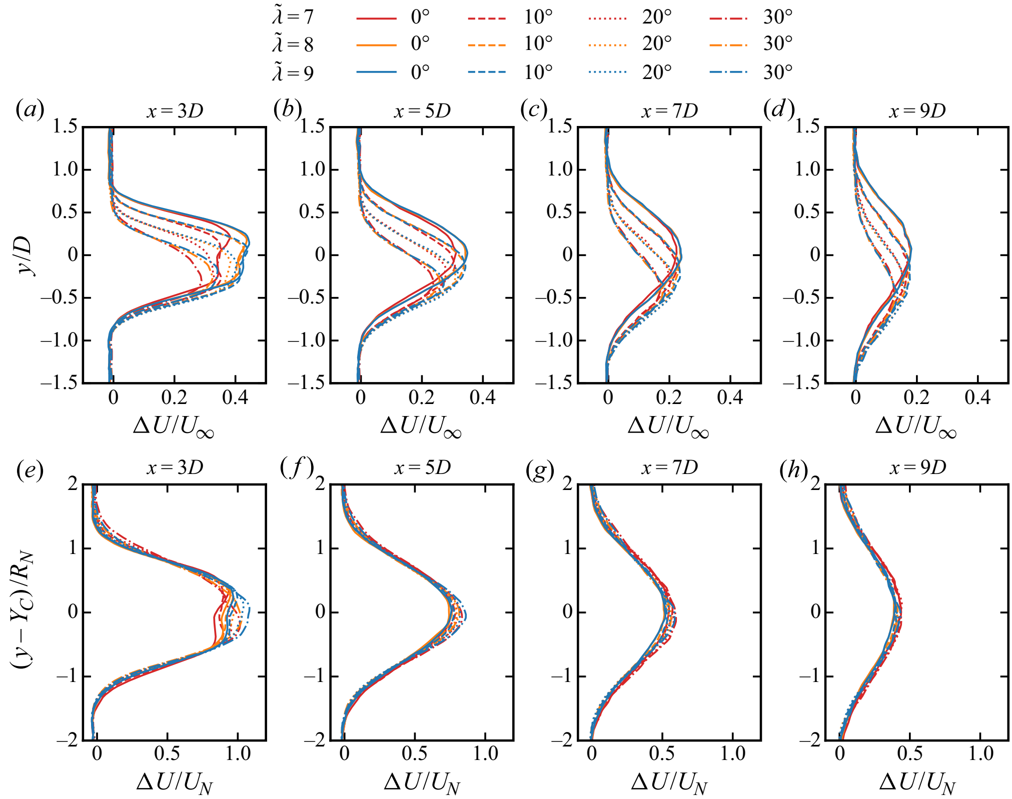

Figure 9. The time-averaged velocity deficit $\Delta U = U_\infty - U$ at downstream locations of ($x \in \{3D, 5D, 7D, 9D\}$) on the hub-height plane ($z = z_{hub}$) for different $\tilde{\lambda}$ and yaw angles: (*a–d*) normalized by the inflow velocity U_∞; and (*e–h*) the wake centres are shifted with respect to Y_C, with the values normalized by the proposed velocity and length scale U_N and R_N.

3.5. *Transverse velocity V*

In this subsection, we investigate the similarity of the transverse velocity V. Recall that in figure 4, the transverse velocity field is shown to be significantly different from the streamwise velocity and is thus not expected to have the same characteristic velocity and length scales. Consequently, the characteristic quantities scales defined using the transverse component of the thrust T_y, following Jiménez *et al.* (2010) and Shapiro *et al.* (2018), will be employed for scaling the quantities related to the transverse velocity, i.e. $R^V_{1/2}(x)$ and $V_C(x)$. Because the transverse velocity is induced by the CVP in the wake (Bastankhah & Porté-Agel 2016; Howland *et al.* 2016), the transverse profiles of V are fitted with a CVP shape function derived based on the Biot–Savart law instead of the Gaussian function (see Appendix E for details).

We first examine the wake half-width $R^V_{1/2}(x)$ defined using the transverse profiles of the transverse velocity. Figure 10 shows the streamwise variation of $R^V_{1/2}$. Recall that both wake expansion and yaw can induce transverse velocity near the rotor, as shown in figure 4, so using the fitting function based on the CVP to define $R^V_{1/2}$ works only in the far wake ($x > 4D$). Despite some fluctuations, it is found that the variation of $R^V_{1/2}(x)$ with yaw angles is smaller than that of $R_{1/2}$. The curves of the same $\tilde{\lambda}$ cluster together, which shows

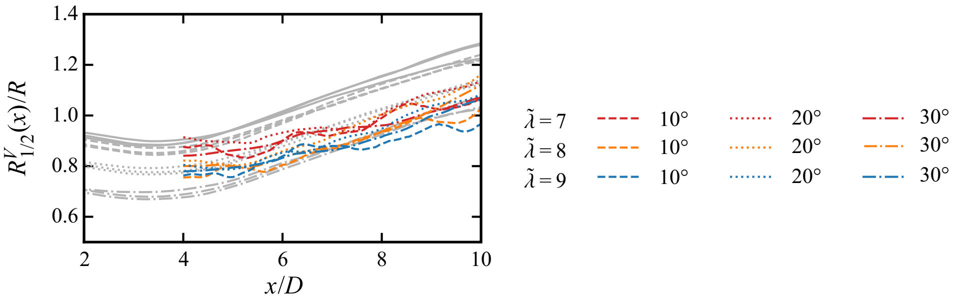

Figure 10. Streamwise variations of the half-width $R^V_{1/2}(x)$ computed by fitting the transverse profiles of the transverse velocity V. The grey curves replot $R_{1/2}(x)$ computed from the streamwise velocity in figure 8(a) for comparison.

that $R^V_{1/2}(x)$ is less dependent on the yaw angle. The yaw-independent scaling of $R^V_{1/2}$ is consistent with the theory of Glauert (1926) for auto-gyros, where the initial influencing zone of V is found to have the same size as the rotor disc instead of the projected size of the rotor disc (Burton *et al.* 2011). The fluctuations of $R^V_{1/2}$ may be explained by the complex dynamics related with the transverse velocity, e.g. the CVP and its interaction with the wake rotation (Bastankhah & Porté-Agel 2016; Howland *et al.* 2016). In the far-wake locations ($x > 4D$), both $R^V_{1/2}(x)$ and $R_{1/2}(x)$ gradually increase with the distance from the turbine.

We then examined the similarity of the transverse velocity using the velocity scale V_N, which is proportional to the initial transverse velocity given by Jiménez *et al.* (2010) and Shapiro *et al.* (2018):

$$V_N = \tfrac{1}{2}\tilde{C}_T \cos^2\gamma \sin\gamma\, U_\infty. \tag{3.7}$$

Figure 11 shows the streamwise variations of the maximum transverse velocity $V_C(x)$ obtained from with the CVP fitting function. In figure 11(b), $V_C(x)/V_N$ increases from approximately 0.4 at $x = 2D$ to 0.7 at $x = 4D$ and then gradually decreases to approximately 0.4 at $x = 10D$. More importantly, the V_C/V_N profiles for different γ and $\tilde{\lambda}$ approximately overlap with each other especially at far downstream locations, which shows the characteristic velocity V_N successfully captures the main feature of the similarity. (The standard deviations of the relative differences of the different curves from the mean of the curves shown in figure 11(a,b) are approximately 31 % and 3.5 %, respectively, in the far-wake region ($x > 4D$).) However, there are slightly larger differences between these curves when comparing with U/U_N (figure 7), which implies that V_N does not include all the underlying physics.

In figure 12(a–d), the V profiles are normalized using the incoming wind speed U_∞. For a given $\tilde{\lambda}$, the velocity amplitude increases when increasing the yaw angle for all the considered streamwise locations. At $x = 3D$, the V profiles show complex variations, especially for the cases with a yaw angle $\gamma = 10^\circ$. In figure 12(e–h), the V profiles are normalized by the proposed velocity scale V_N and shifted with respect to the centre location Y_C based on the streamwise velocity deficit. It is noted that scaling of the transverse velocity profiles is not as accurate as that for the streamwise velocity deficit. This is probably because many other factors including the wake rotation and vertical shear, which affect the transverse velocity, are not taken into account in the proposed scaling.

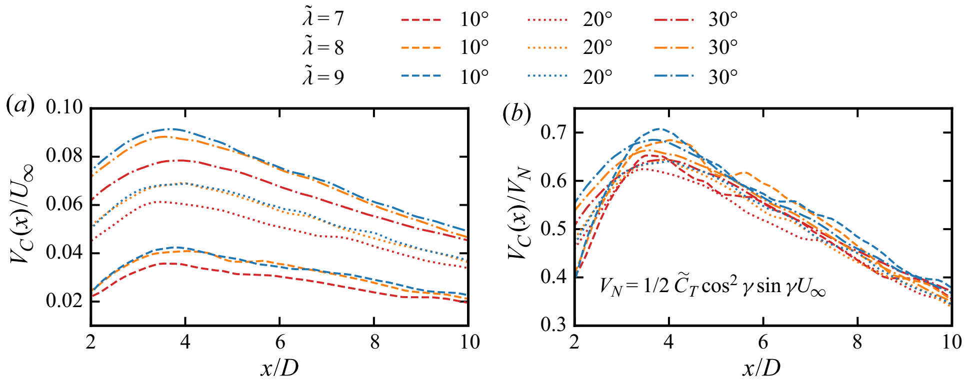

Figure 11. The characteristic transverse velocity $V_C(x)$ for different yaw angles: (*a*) normalized by inflow velocity U_∞; and (*b*) normalized by the proposed velocity scale $V_N = (\tilde{C}_T \cos^2\gamma \sin\gamma U_\infty)/2$.

However, the profiles of the transverse velocity are approximately symmetrical about the peak, and the overall shape can be fitted with the proposed CVP function (the grey curves) especially in the far wake. Additionally, the peak of the transverse velocity locates on one side of the wake centreline Y_C at approximately $0.5D$ and varies slightly with the downstream locations, which was assumed to be approximately equal to S in (3.3) in the paper by Bastankhah & Porté-Agel (2016). This shift of the maximum of the transverse velocity from the wake centreline may explain the overestimation of Y_C computed using a uniform V, as in the analytical wake models of Jiménez *et al.* (2010), as shown by e.g. Bastankhah & Porté-Agel (2016). However, it should also be noticed that the shape of V is different from the idealized shape of the CVP fitting function in the near wake, as shown in figure 13, as a result of complex flow dynamics in the near wake caused by the nacelle, the wake rotation (Bastankhah & Porté-Agel 2016; Howland *et al.* 2016) and the inflow vertical shear (Gebraad *et al.* 2017). The tower, which was not considered in the work, may also have an effect.

4. Similarity of turbulence statistics of yawed turbine wakes

In this section, we examine the turbulence statistics of yawed turbine wakes, which include the turbine-added turbulence kinetic energy, turbine-added Reynolds shear stress and the statistics of instantaneous wakes. This section presents the results of cases with inflow 1. The influence of inflow turbulence will be discussed in § 5.

4.1. *Turbine-added turbulent kinetic energy and Reynolds shear stresses*

In this subsection, we examine the similarity of the turbine-added turbulence kinetic energy Δk and the turbine-added Reynolds shear stresses $\Delta\langle u'v'\rangle$ and $\Delta\langle u'w'\rangle$. The employed characteristic velocity scale is given as follows:

$$U_T = U_\infty \cos\gamma \sqrt{\tilde{C}_T/2}. \tag{4.1}$$

Figure 13 shows the streamwise velocity deficit, the turbine-added turbulence kinetic energy and Reynolds shear stresses at $x = 7D$ for cases of different yaw angles with $\tilde{\lambda} = 8$. The streamwise velocity deficit is plotted in figure 13(*a*–*d*), to illustrate the wake region. The wake centre is shown to be deflected to the left and the wake's cross-section

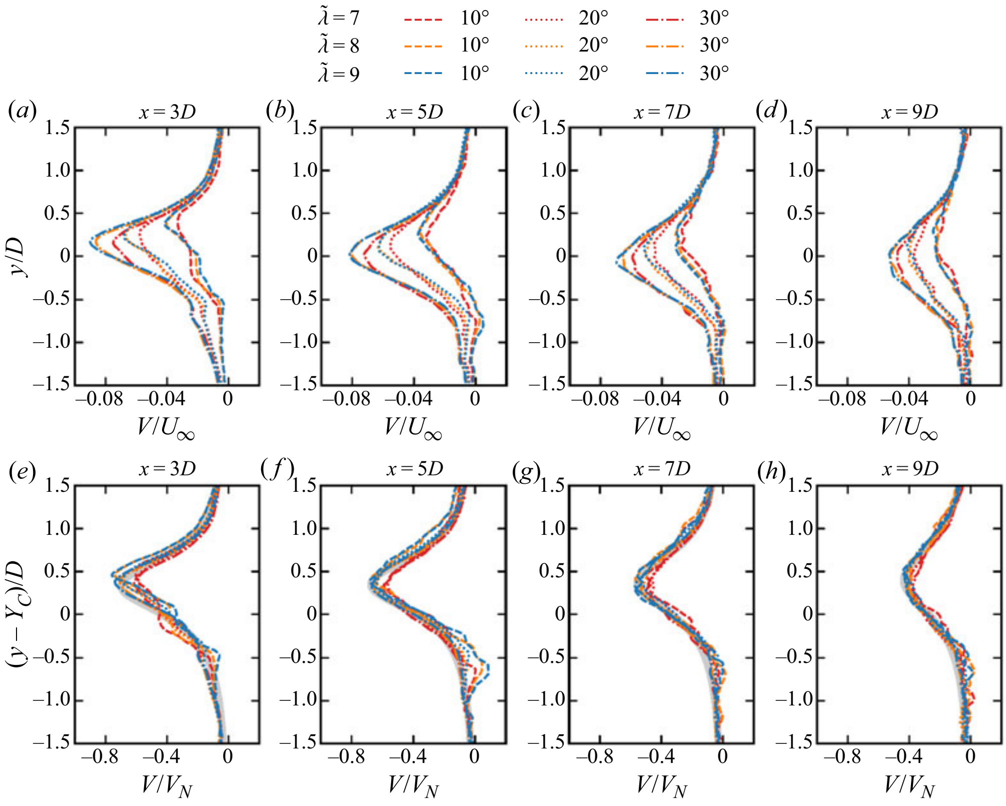

Figure 12. The time-averaged transverse velocity V profile at downstream locations of ($x \in \{3D, 5D, 7D, 9D\}$) on the hub-height plane ($z = z_{hub}$) for different yaw angles: (*a–d*) V normalized by the inflow velocity U_∞; (*e–h*) the wake centres are shifted with respect to Y_C, with the values normalized by the velocity scale $V_N = (\tilde{C}_T \cos^2\gamma \sin\gamma U_\infty)/2$. The grey thick curves show the corresponding fitting function.

is deformed to a curled-shape with top-down asymmetry when increasing the yaw angle, as described in the literature (Howland *et al.* 2016). Interestingly, the curled-shape is less obvious for the turbine-added turbulence kinetic energy Δk , which shows an approximate left-right symmetry, as shown in figure 13(*e–h*). The turbine-added Reynolds shear stress $\Delta\langle u'v'\rangle$ is plotted in figure 13(*i-l*) and $\Delta\langle u'w'\rangle$ is plotted in figure 13(*m–p*). Overall it is found that these Reynolds stresses become asymmetric at large yaw angles. Moreover, it is found that $\Delta\langle u'v'\rangle > \Delta\langle u'w'\rangle$, which may be related to the stronger horizontal wake meandering. In the following, the transverse profiles of Δk and $\Delta\langle u'v'\rangle$ at the hub height and different streamwise locations will be examined in detail for different yaw angles and turbine operation conditions. The vertical profiles $\Delta\langle u'w'\rangle$, however, will not be be examined because of its irregular shape and the difficulty to define the location for comparison.

Figure 14 compares the turbine-added turbulence kinetic energy Δk computed from cases with different γ and $\tilde{\lambda}$ at different downstream locations. The curves in figure 14(*a–d*) are Δk profiles normalized using U^2_∞. Here, the Δk profiles of different yaw angles show apparent differences in terms of the magnitude, the locations of the Δk peaks and the width of the zone with increased turbulence. Figure 14(*e–h*)show the same results with the abscissa scaled by U^2_T and the ordinate shifted with $Y_C(x)$ then scaled

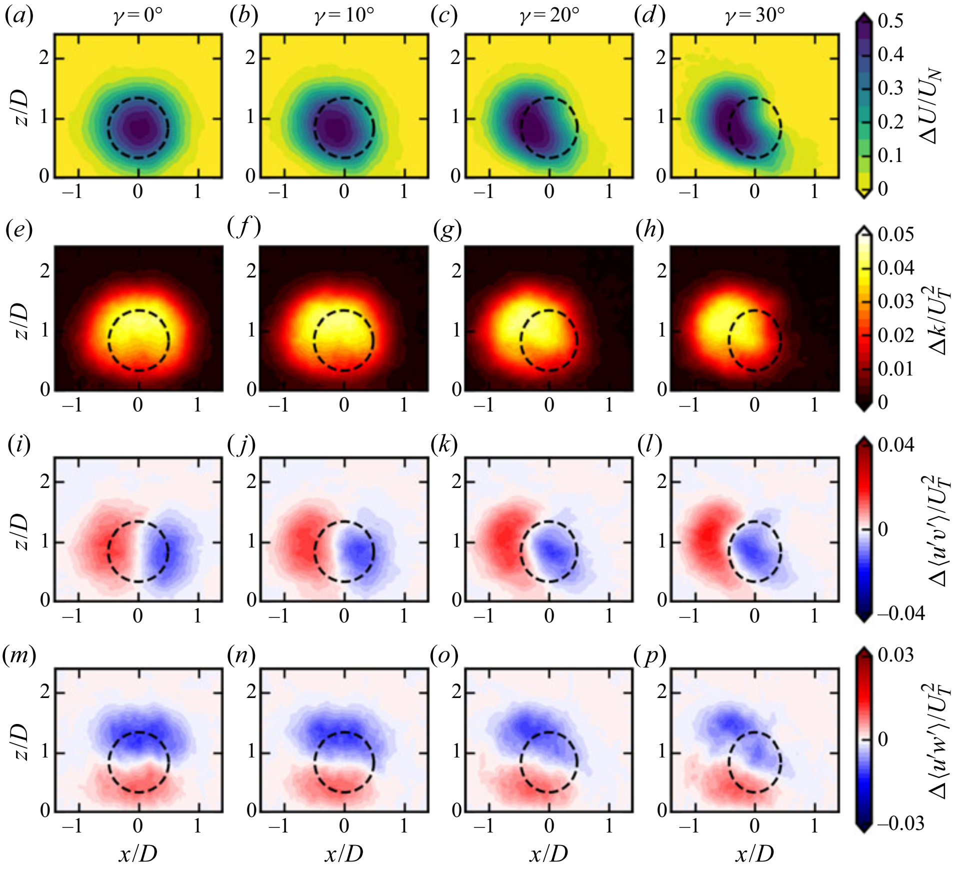

Figure 13. Wake characteristics at $x = 7D$ for cases of different yaw angles with $\tilde{\lambda} = 8$: (*a–d*) the streamwise velocity deficit ΔU; (*e–h*) the turbine-added turbulence kinetic energy Δk; (*i–l*) the turbine-added Reynolds shear stress $\Delta\langle u'v'\rangle$; and (*m–p*) the turbine-added Reynolds shear stress $\Delta\langle u'w'\rangle$. The dashed circles illustrate the projected rotor.

by R_N. With this scaling, the Δk profiles of different yaw angles overlap with each other in the far wake, which shows that the characteristic velocity U_T is still the proper velocity scale for the wake of yawed wind turbines. By further probing into the Δk profiles in the near wake, it is found that the profile of Δk contains two peaks with the distance between the two peaks scaled well by R_N, as the location of Δk peaks appear at $Y_C \pm S$, which is consistent with results in the literature (Schottler *et al.* 2018). It is also observed that Δk in the near wake ($x = 3D$, figure 14*a*,*e*) is asymmetric when $\gamma \neq 0°$ (especially for $\gamma = 30°$) and Δk behind the trailing half of the rotor ($y - y_C < 0$) is larger than that behind the leading half ($y - y_C > 0$), which is similar to the flow passed an inclined circular disc (Calvert 1967; Gao *et al.* 2018). This asymmetry increases with γ and cannot be captured by the proposed velocity scale U_T. However, it only manifests in the near wake and may be considered as immaterial in utility-scale wind farms, where the turbine spacing is often larger than 5D (Méchali *et al.* 2006). At far-wake locations, this asymmetry disappears with the $\Delta k/U_T^2$ profiles overlapping well with each other on the $(y - Y_C)/R_N$ coordinate.

Figure 15 plots the turbine-added Reynolds shear stress $\Delta\langle u'v'\rangle$ at the hub-height plane ($z = z_{hub}$) presented in the same manner as figure 14. In figure 15(*a*), it is observed that

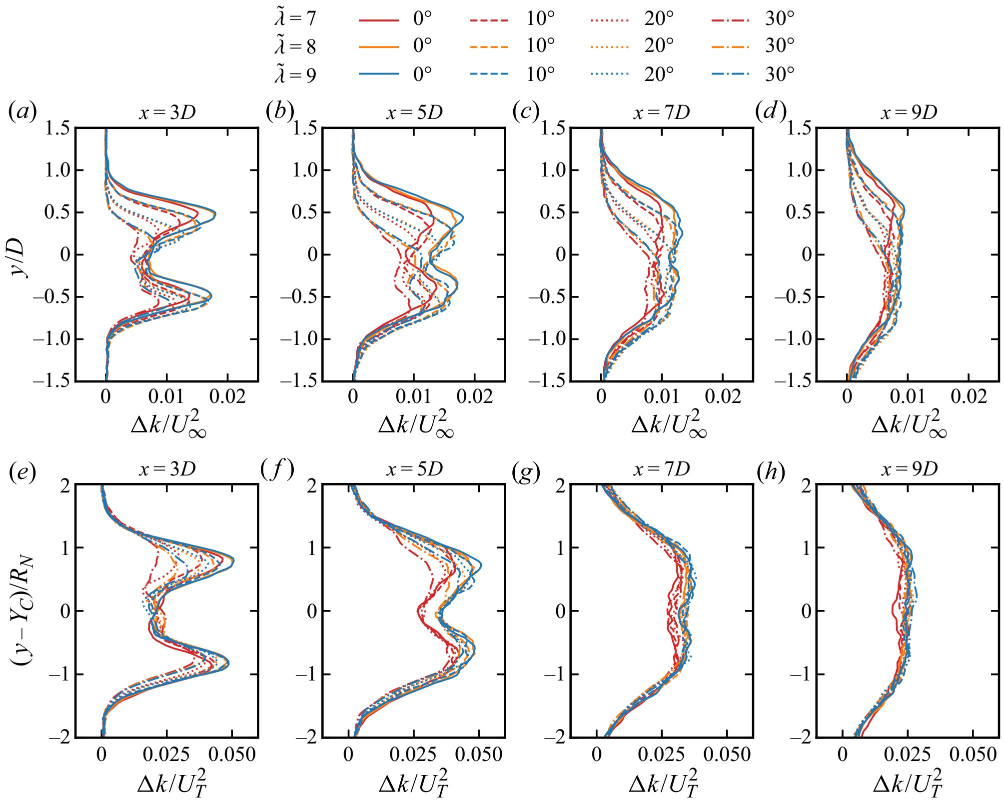

Figure 14. The turbine-added turbulence kinematic energy Δk at downstream locations of ($x \in \{3D, 5D, 7D, 9D\}$) on the hub-height plane ($z = z_{hub}$) for different yaw angles and $\tilde{\lambda}$: (*a–d*) normalized by the square of the inflow velocity U_∞^2; (*e–h*) the wake centres are shifted with respect to Y_C and normalized by the length scale R_N, with the values normalized by the square of the velocity scale U_T^2.

$\Delta\langle u'v'\rangle$ profiles are featured by complex variations near the wake centre at $x = 3D$, which is caused by the turbine nacelle and root loss near the hub. When $\Delta\langle u'v'\rangle$ are plotted on the coordinate $(y - Y_C)/R_N$, the turbine-added Reynolds shear stress profiles normalized using U_T^2 overlap with each other in the far wake ($x \geq 5D$) for different yaw angles and $\tilde{\lambda}$, which confirms U_T as the proper velocity scale for the turbine-added Reynolds stresses.

4.2. *Statistics of instantaneous wake centre and width*

This subsection analyses the influence of the yaw misalignment on the dynamics of the horizontal large-scale wake motion (wake meandering), which has a significant impact on the wake expansion, recovery and the fatigue loads on downstream wind turbines (Ainslie 1988; Högström *et al.* 1988; Larsen *et al.* 2007). In the same way as for the time-averaged wake centre, the instantaneous wake centre is defined as the centre of the Gaussian fit of the instantaneous velocity deficit, which is obtained by subtracting the velocity field computed from the case without wind turbines at exactly the same instant. Figure 16 shows the velocity deficit behind a turbine with $\gamma = 0^\circ$ and a turbine with $\gamma = 30^\circ$ at the same instant. To obtain the wake centre position and the width along the downstream locations, the velocity deficit ΔU profile is first spatially filtered with a width of $0.5D$ in the streamwise direction (x) and then is fitted to the Gaussian function at each downstream

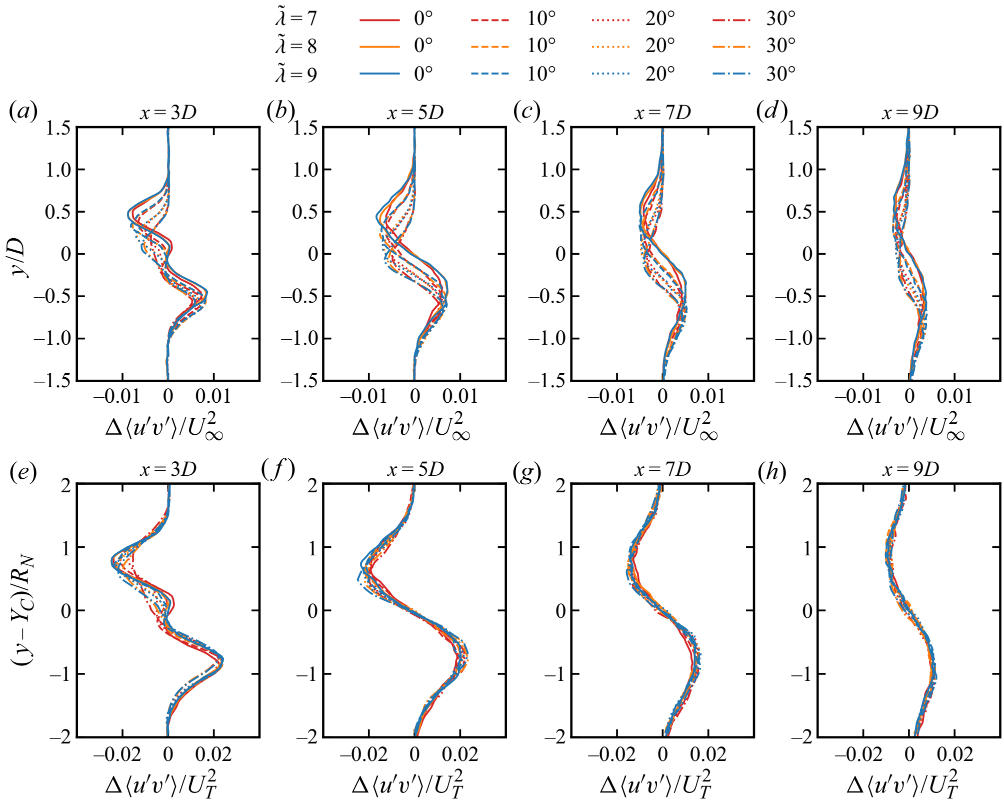

Figure 15. The turbine-added Reynolds shear stress $\Delta\langle u'v'\rangle$ on the hub-height plane ($z = z_{hub}$): (*a–d*) normalized by the square of the inflow velocity U_∞^2; (*e–h*) the wake centres are shifted with respect to Y_C and normalized by the length scale R_N, with the values normalized by the square of the velocity scale U_T^2. For the legend, see figure 14.

location with (3.3). The curve_fit function in the scipy.optimize package is employed for the fitting process. At each time step, the fitting starts from the near wake with the fitting results serving as the initial guess for the next downstream location to help to converge the fitting process. The filtered velocity deficit and the fitted Gaussian curve are illustrated in figure 16(*b*) for $\gamma = 0^\circ$ and figure 16(*d*) for $\gamma = 30^\circ$ both with $\tilde{\lambda} = 8$. Despite some fluctuations in the instantaneous velocity profiles (blue lines), the fitted Gaussian curves (red dashed lines) capture the wake centre position y_c and width $r_{1/2}$ satisfactorily. In figure 16(*a*,*c*), the fitted wake centre lines $y_c(x)$ and the characteristic wake half-width (defined by $r_{1/2}(x)$) are plotted with red dotted lines and red dashed lines, respectively. Generally, they provide a good estimation of the overall trend of the wake in the entire region except for $9D < x < 10D$, where the velocity deficit is small and irregular. It is found that the wake behind a yawed wind turbine is generally narrower and that the velocity deficit is smaller than the wake behind a non-yawed turbine. This observation is in accordance with the time-averaged wake quantities. In the following, we examine whether the proposed scales for the time-averaged wake are still appropriate for the statistics of the instantaneous wakes. The following analyses in this section are based on the data collected on the horizontal plane located at the turbine hub height with inflow 1.

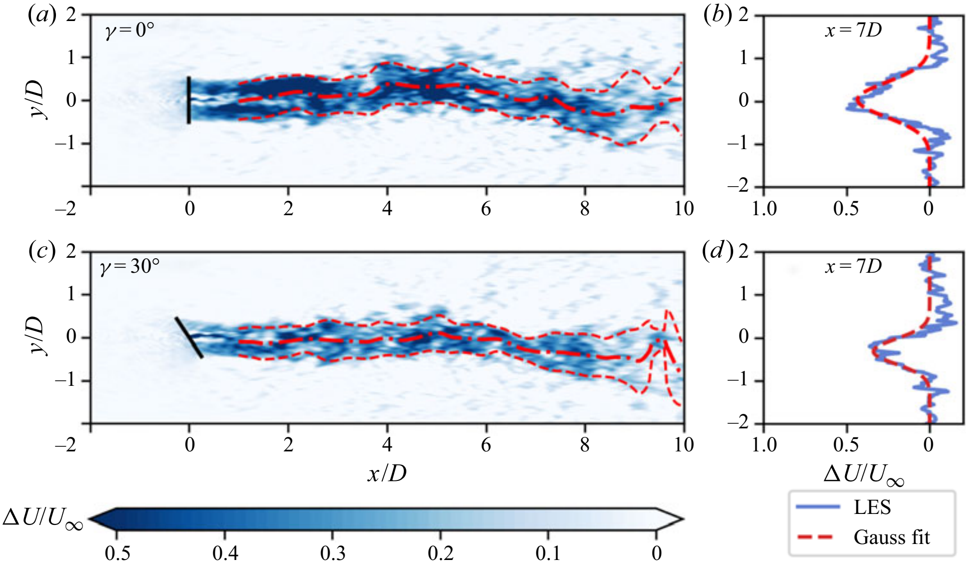

Figure 16. Instantaneous flow field behind the wind turbines at hub-height plane $z = z_{hub}$. The contour of the velocity deficit ΔU at the same simulation time for yaw angles $\gamma = 0°$ (*a*) and $\gamma = 30°$ (*c*). The black solid lines illustrate the wind turbines. Red dash–dotted lines denote the wake centreline $y_c(x)$ and the red dashed lines denote the wake width defined by $r_{1/2}(x)$ obtained from the Gaussian fit of the instantaneous streamwise velocity. The velocity deficit at $x = 7D$ and the corresponding Gaussian fit for yaw angles $\gamma = 0°$ (*b*) and $\gamma = 30°$ (*d*).

We first show the probability density function (p.d.f.) of the wake centre location at $x \in \{5D, 7D, 9D\}$ for different yaw angles in figure 17. In this figure, panels in the same rows are at the same downstream location and the panels in the same columns are at the same yaw angle. For brevity, only the results of $\tilde{\lambda} = 8$ are plotted as the results of all considered $\tilde{\lambda}$ were similar. The p.d.f. is plotted as grey bars and is fitted to normal distribution curves. In each panel, two vertical lines are plotted to denote the wake centreline location obtained from the time-averaged velocity field (Y_C) and the mean value of the instantaneous centre location ($\overline{y_c}$), respectively. These two lines overlap. When increasing the yaw angle, the p.d.f. moves in the $-y$ direction owing to the wake deflection. In the last column, the p.d.f. profiles for the different yaw angles are shifted with respect to Y_C and plotted in the same figure, and are shown to overlap with each other. This indicates that the transverse distribution of the instantaneous wake centres is independent of the yaw angle at different downstream locations for the present cases, which further indicates that the amplitude of wake meandering, defined as the standard deviation of the wake centre location, does not change with yaw angle. By comparing the p.d.f.s at different locations, it is found that the wake centres distribute in a wider range as the wake travels downstream, which is in accordance with the wake expansion phenomenon. It is also noted that the p.d.f. distribution is not exactly Gaussian. To examine this, we compute the skewness of the distribution in table 3. The skewness for cases with non-zero yaw angles generally has a positive value, which shows that the distribution has a longer tail on the right (Lovric 2011), i.e. in the opposite direction of the mean wake deflection. However, because these skewness is rather small (in the range of −0.5 to 0.5), the distribution is thus approximately symmetrical and can be approximated by the normal distribution (Cramer 2002).

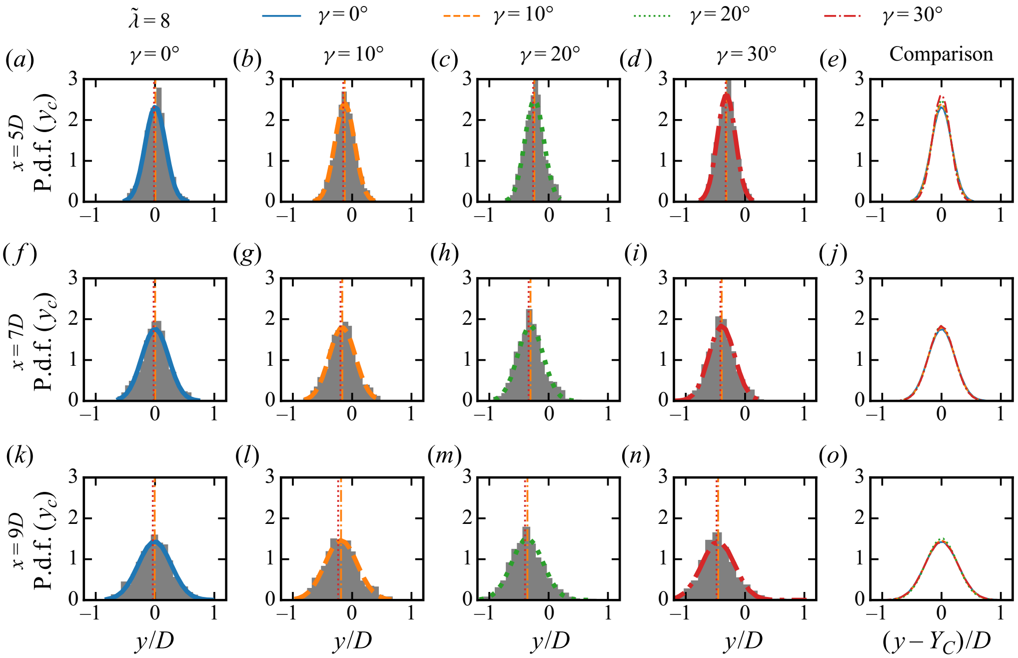

Figure 17. The probability density function of the instantaneous wake centre at $x \in \{5D, 7D, 9D\}$ for different yaw angles at $\tilde{\lambda} = 8$. The histogram is fitted to a Gaussian distribution function in each panel, and the fitted curves are compared in panels (*e*,*j*,*o*). The orange dashed vertical lines denote the mean value of the instantaneous wake centre locations and the red dotted vertical lines are plotted at the wake centre obtained from the time-averaged velocity shown in figure 6.

	$\gamma = 0°$	$\gamma = 10°$	$\gamma = 20°$	$\gamma = 30°$
$x = 5D$	0.013	−0.045	0.079	0.039
$x = 7D$	0.015	0.037	0.271	0.126
$x = 9D$	0.073	0.223	0.273	0.193

Table 3. The skewness of the instantaneous wake centre position y_c for different yaw angles. The skewness is defined as $g_1 = m_3/\sigma_{y_c}^3$ with $m_3 = (1/N)\sum_{i=1}^{N}(y_c - \overline{y_c})^3$ and N is the number of samples.

Similarly, the p.d.f.s of the instantaneous wake width $r_{1/2}$ are compared in figure 18. The peak of the p.d.f. is found to move towards the left when increasing the yaw angle, which indicates that the wake width decreases with yaw angle. Travelling downstream, the peak moves slightly to the right owing to the wake expansion. For the cases with yaw angles $\gamma = 0°$ and $10°$, the distributions of $r_{1/2}$ are well represented by the normal distribution, while for the cases with $\gamma = 20°$ and $30°$, the p.d.f.s are slightly skewed with a longer right tail especially at $x = 9D$. On the other hand, the standard deviation of $r_{1/2}$ is not greatly affected by the yaw angles, as observed in the last column.

We further analyse the streamwise evolution of instantaneous wake characteristics at different γ and $\tilde{\lambda}$. In figure 19(*a*), the streamwise variations of $\overline{y_c}$ computed from different yaw angles and $\tilde{\lambda}$ are compared. The mean of the instantaneous wake centre locations is shown to scale well using the proposed length scale Y_N and agrees with the wake centre

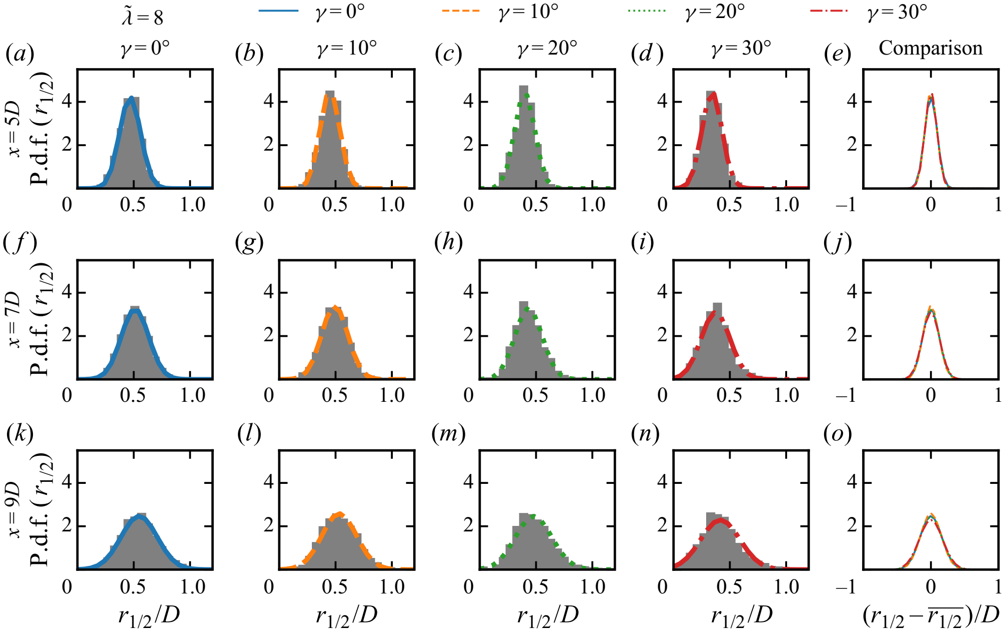

Figure 18. The probability density function of the instantaneous wake width at $x \in \{5D, 7D, 9D\}$ for different yaw angles at TSR $\tilde{\lambda} = 8$. The histogram is fitted to a Gaussian distribution in each panel, and the fitted curves are compared in panels (*e*,*j*,*o*).

obtained from the time-averaged field Y_C (in grey). Figure 19(*b*) plots the streamwise evolution of the standard variation of the wake centre position σ_{y_c}, which indicates the amplitude of the meandering motion of the wake centre around its mean position. In figure 19(*b*), the rotor diameter D, instead of Y_N, is used for the normalization. Here, the σ_{y_c} for the different cases overlap with each other. This observation further confirms the finding from the p.d.f. of the wake centre in figure 17, where the wake meandering amplitudes are independent of yaw angle and TSR. Furthermore, it is observed that σ_{y_c} increases approximately linearly with the distance to the turbine, which shows that the meandering amplitude increases as the wakes travel downstream, and this conforms with Taylor's frozen eddy hypothesis.

The instantaneous wake width $r_{1/2}$ is analysed in figure 19(*c*,*d*). From figure 19(*c*), it is found that the mean value of the instantaneous wake width $\overline{r_{1/2}(x)}$ for different γ and $\tilde{\lambda}$ can be properly scaled by the proposed length scale R_N. When compared with the time-averaged wake width $R_{1/2}(x)$ shown in grey, the widths defined by both approaches agree well in the near wake ($x = 1D$), then $R_{1/2}$ becomes larger at further downstream locations. This is because $R_{1/2}$, defined using the time-averaged velocity field, combines both the expansion of the instantaneous wake width $r_{1/2}$ and the wake meandering, and the latter smears the instantaneous velocity deficit over a wider region; in contrast, the wake width follows the instantaneous wake centre y_c and expands slower. The difference between $r_{1/2}$ and $R_{1/2}$ increases with turbine downstream distance in accordance with the meandering amplitude represented by σ_{y_c}. Figure 19(*d*) plots the standard deviation of the instantaneous wake half-width $\sigma_{r_{1/2}}$, which represents the wake deformation that expands and shrinks with time. It is noticed that the standard deviations of the wake

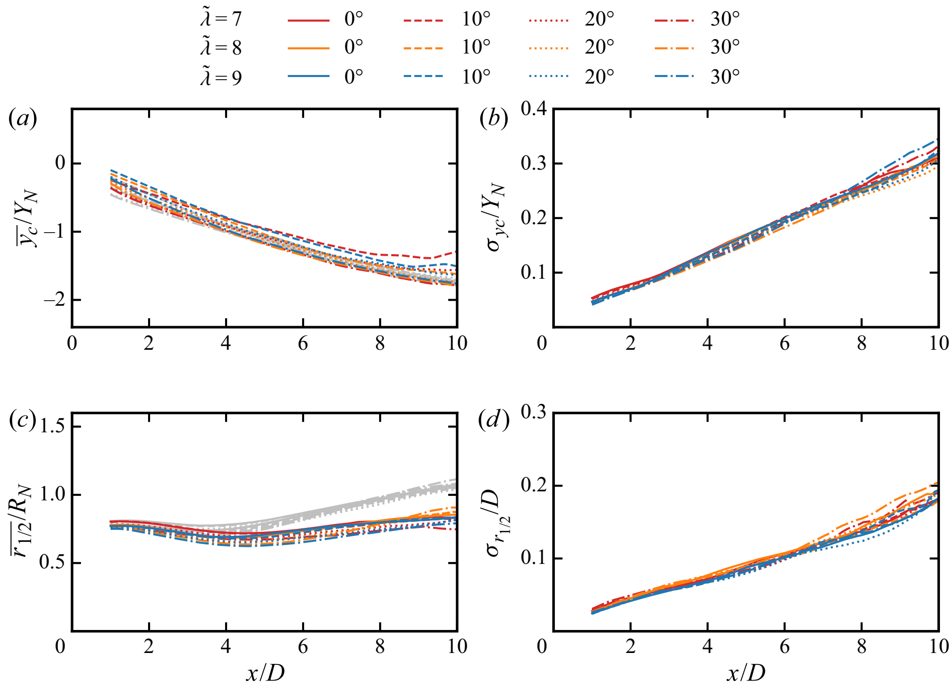

Figure 19. Streamwise distribution of the statistics of instantaneous quantities of the wakes behind yawed wind turbines, where the values are scaled with the same factors as for the time-averaged quantities: (*a*) the mean value of instantaneous wake centre positions $y_c(x)$, scaled by Y_N; (*b*) the standard deviation of $y_c(x)$ normalized by the rotor diameter D; (*c*) the mean value of the characteristic instantaneous wake width $r_{1/2}(x)$ scaled by R_N; (*d*) the standard deviation of $r_{1/2}(x)$ normalized by D. In (*a*,*c*), the grey curves plot the corresponding normalized characteristics obtained from the time-averaged velocity field.

width for different yaw angles and $\tilde{\lambda}$ overlap with each other when normalized by the rotor diameter D, which suggests again that the wake deformation is not greatly influence by the turbine operation condition. Furthermore, the standard deviation of $r_{1/2}$ gradually increases travelling in the streamwise direction, which indicates a larger wake deformation in the far wake.

In summary, figure 19 mainly reveals that the mean of the instantaneous wake quantities and their standard deviation are scaled differently. The proposed scaling factors derived for the time-averaged velocity field still work for the mean value of y_c, $r_{1/2}$, but the standard deviations of these quantities, on the other hand, are independent of the length scales defined using the turbine operation condition. The influence of inflow turbulence on the meandering amplitude and the wake deformation will be analysed in detail in § 5.

5. Effects of inflow turbulence

In this section, the simulation results for cases with $\tilde{\lambda} = 8$, $\gamma = \{0^\circ, 10^\circ, 20^\circ, 30^\circ\}$ and the three different turbulent inflows are examined to probe the influence of the inflow turbulence on the wake characteristics and the proposed velocity and length scales. Recall that the three turbulent inflows denoted as inflow 1, inflow 2 and inflow 3 have the same normalized mean streamwise at the turbine's hub height and their turbulent intensities are equal to 6.9 %, 7.9 % and 9.6 %, respectively.

5.1. *Characteristics of the time-averaged wake*

Figure 20 shows the characteristics of the time-averaged wake for different yaw angles and different inflow conditions. In figure 20(*a*), the wake centreline deflection is compared. When comparing curves from the cases with the same inflow, the wake deflections $Y_C(x)$ for the cases with different yaw angles overlapped with each other when normalized by Y_N. Furthermore, a reduction of the wake deflection was observed at far-wake locations when the inflow turbulence intensity was increased, which is in agreement with previous studies (Jiménez *et al.* 2010; Bastankhah & Porté-Agel 2016; Bartl *et al.* 2018). Furthermore, the spanwise velocity $V_C(x)$ in figure 20(*b*) was found to decrease with increasing inflow turbulence intensity and the normalized values in general agreed with each other for the same inflow. The influence of the inflow turbulence on the streamwise velocity deficit is shown in figure 20(*c*). The normalized streamwise velocity deficits $\Delta U_C(x)/U_N$ showed a remarkably good agreement between different yaw angles, but they decreased with the turbulence intensity. Moreover, all the curves started at similar y intercepts at approximately 1 in the near wake, which showed that the effect of the inflow turbulence on the imminent wake is minor, where the streamwise velocity deficit can be predicted well by the one-dimensional momentum theory. In contrast, the effect of the inflow condition becomes important in the far wake, where it affects wake recovery, as reported in the literature (Bastankhah & Porté-Agel 2017). The length of the near-wake region can be defined using the maximum streamwise velocity deficit. The so-computed near-wake region is shown in figure 20(*d*). Interestingly, it is found that increasing the yaw angle and inflow turbulent intensity both result in a shorter near-wake region, with a larger impact from the inflow turbulence. The streamwise variation of the wake width $R_{1/2}$ is shown in figure 20(*e*). The curves overlap well with each other in the near wake regardless of the inflows. Beyond this near-wake region, the wake expands approximately linearly. For the cases with higher turbulence intensity, the wake width is also larger as the wake expansion starts earlier and grows faster. It is also worth noting that small discrepancies of the normalized wake width for different yaw angles are observed in the far wake at $x > 6D$, especially for the inflow 3 cases with the highest turbulence intensity. This indicates that the length scale R_N, which is derived from the one-dimensional momentum theory, may encounter difficulties to scale the far-wake width when the inflow turbulence intensity is high.

The transverse profiles of the streamwise velocity deficit ΔU and the transverse velocity V are presented in figure 21. In general, these results confirm that the proposed scaling factors are able to overlap the profiles of different yaw angles for the same inflow, and that the magnitudes of the turbine induced streamwise velocity deficit ΔU and the transverse velocity V decrease faster for inflows with higher turbulence intensity.

5.2. *Characteristics of instantaneous wakes and the turbine-added turbulence*

The statistics of the turbine-added turbulent characteristics, which include the added TKE Δk, and the added Reynolds shear stress $\Delta\langle u'v'\rangle$ are plotted in figure 22. These curves are normalized by the proposed velocity scale U_T and R_N, as in § 4. In general, these curves have similar shapes regardless of the incoming flow. Under the same inflow condition, the curves overlap, which indicates that the proposed velocity and length scales can still describe the similarity of these characteristics for different yaw angles. Because these scales do not consider the influence of the inflow condition, discrepancies between the curves from cases with different inflows are observed, as expected. For Δk, the influence

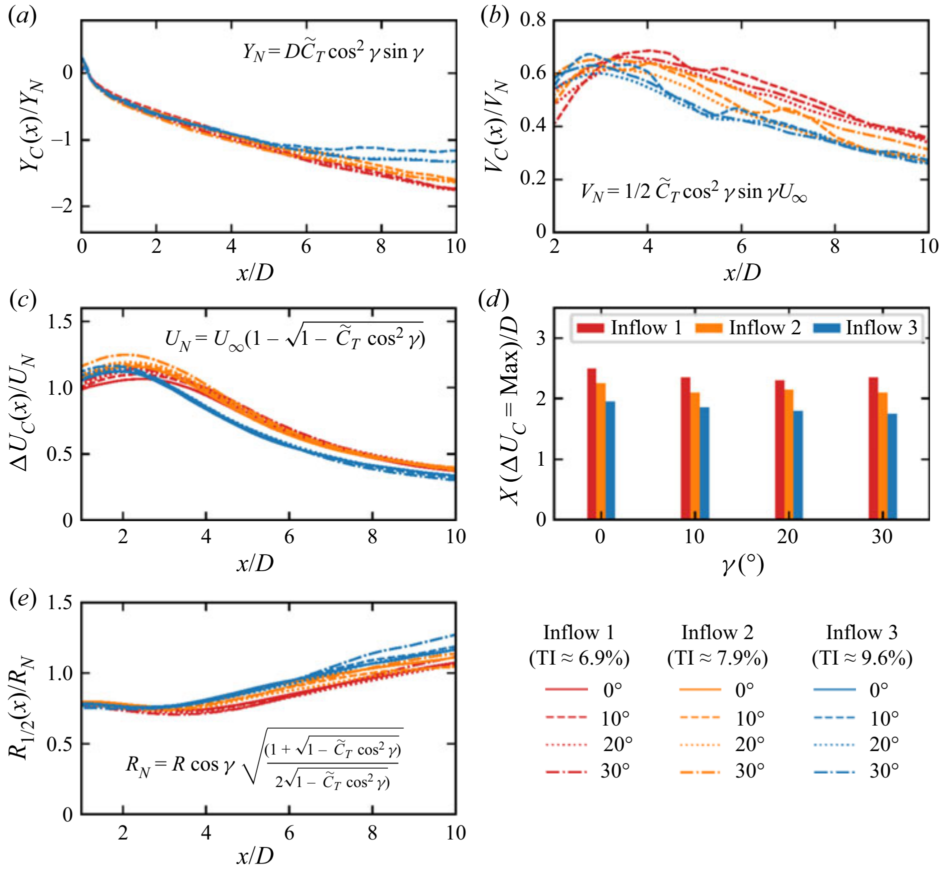

Figure 20. Effects of inflow turbulence on the statistics of time-averaged wakes: (*a*) the centreline deflection; (*b*) the characteristic spanwise velocity; (*c*) the characteristic streamwise velocity deficit; (*d*) near-wake length defined using the streamwise location where the velocity deficit reaches the maximum; and (*e*) the width of the wake.

of inflow is the most obvious at $x = 7D$, where the added TKE decreases when the inflow is changed from inflow 1 and inflow 2 to inflow 3, which is in agreement with the work of Crespo & Herna (1996). For the added Reynolds stress $\Delta\langle u'v'\rangle$, an overall good scaling is observed for the cases under different inflows.

The effects of inflow conditions on the instantaneous wake quantities are examined in figure 23. The same technique explained in § 4 is employed to extract the instantaneous wake quantities from the flow field for the three inflow conditions. In figure 23(*a*), the mean of the instantaneous wake centre location $\overline{y_c}/Y_N$ as a function of downstream location is compared with the wake centreline Y_C/Y_N obtained from the time-averaged velocity field. The mean wake centrelines defined by these two approaches agree fairly well with each other even in the far wake. Figure 23(*b*) shows the standard deviations of the instantaneous wake position for different inflows, as in § 4. It is seen that $\sigma_{y_c}(x)$ is independent of yaw angle for the considered cases. Considering that $\sigma_{y_c}(x)$ essentially represents the meandering amplitude, the observation in figure 23(*b*) suggests that the wake meandering is dominated by the incoming large eddies instead of turbine operation for the present cases, which is consistent with the works of Bastankhah & Porté-Agel (2017) and Yang &

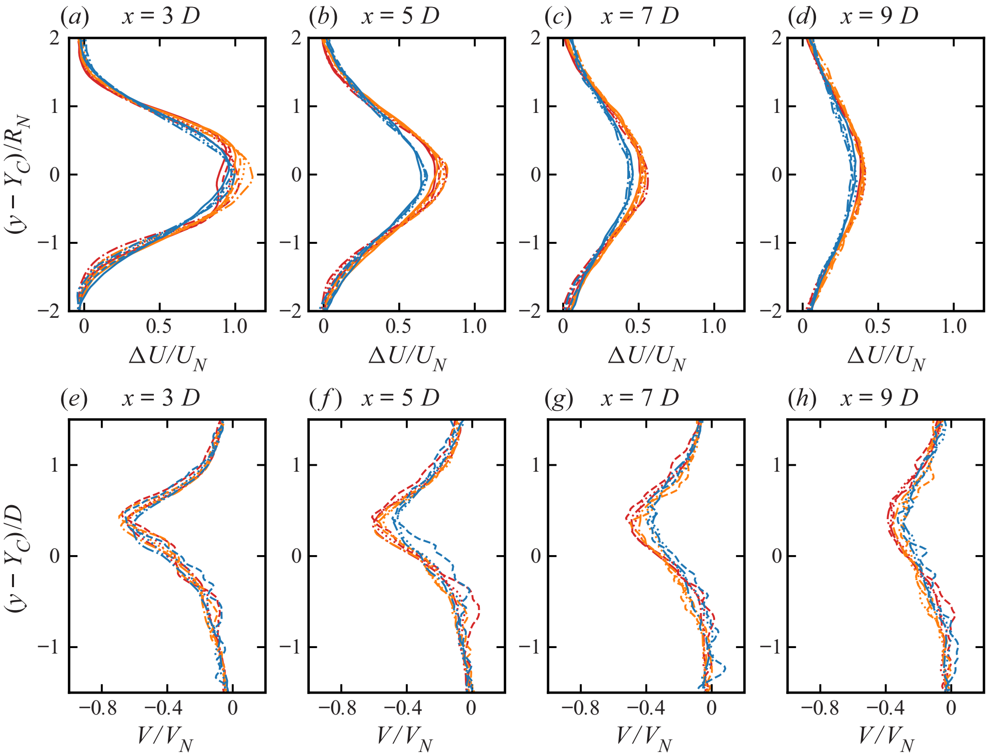

Figure 21. Effects of inflow turbulence on horizontal profiles of the normalized time-averaged wake velocity: (*a–d*) the streamwise velocity deficit; and (*e–h*) the spanwise velocity. See figure 20 for the legend.

Sotiropoulos (2019*b*). Figure 23(*c*) compares the mean of the instantaneous wake width $\overline{r_{1/2}}$ with the wake width obtained from the time-averaged velocity field $R_{1/2}$ (plotted in grey). The normalized instantaneous wake widths $\overline{r_{1/2}}/R_N$ overlap well with each other for all the considered inflow conditions and yaw angles, which shows that the near-wake width R_N is a good scaling factor even in the far wake. Moreover, the mean of the instantaneous wake width grows very slowly at all the considered locations ($1D < x < 10D$), which suggests that the expansion of the instantaneous wake width is much weaker than that of the time-averaged wake. This should be taken into account in wake meandering models (e.g. the dynamic wake meandering model Larsen *et al.* 2008). Furthermore, it is observed that the instantaneous wake widths are not very sensitive to the inflow condition, i.e. the effects of the inflow turbulence on the expansion of the instantaneous wake are negligible for the considered cases. This further suggests that the faster recovery of the time-averaged wake for cases with higher inflow turbulence intensity is mainly caused by stronger meandering motions. Lastly, the effects of inflow on the standard deviation of the instantaneous wake width are shown in figure 23(*d*). Here, $\sigma_{r_{1/2}}$ is shown to have a similar behaviour to σ_{y_c}, i.e. it increases linearly with downstream distance, and the slope of the increase is nearly independent of turbine yaw angles but increases with the turbulence intensity of the inflow, which indicates stronger instantaneous wake deformation for higher inflow turbulence intensities. Moreover, this figure clearly reveals that increasing the inflow turbulence intensity (TI) leads to an increase in the growth rates of both σ_{y_c} and $\sigma_{r_{1/2}}$. The empirical formula for the dependence of the expansion rate of the

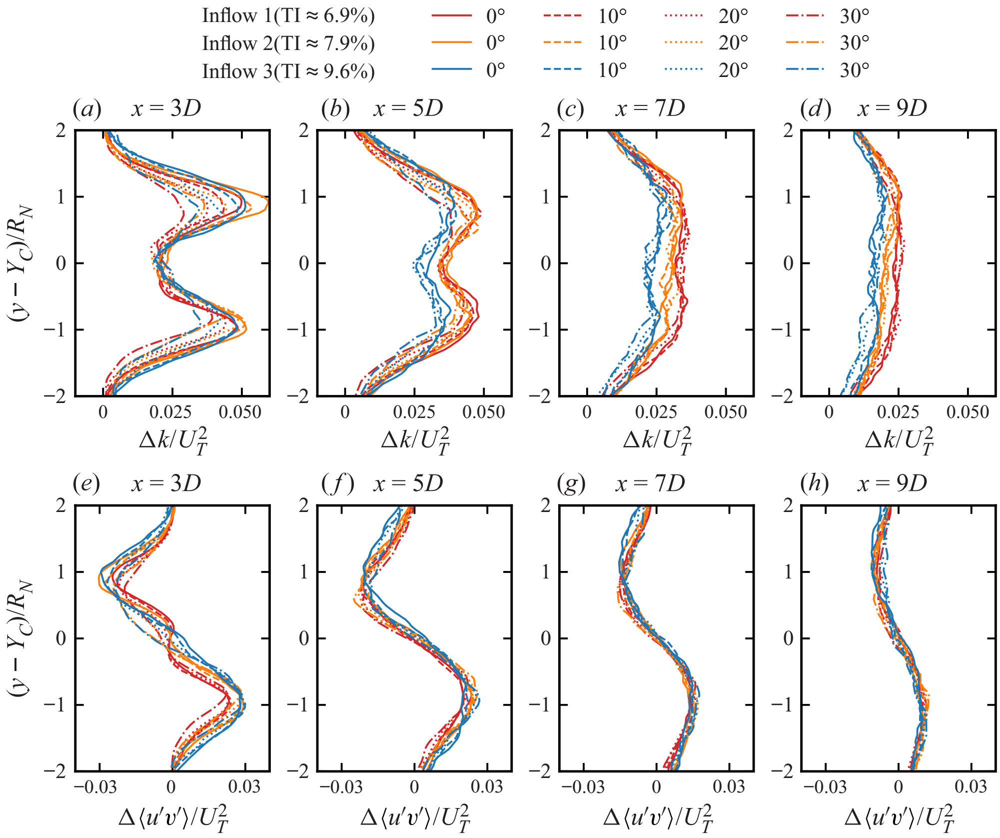

Figure 22. Effects of inflow turbulence on the normalized added turbulence: (*a–d*) the added kinetic turbulent energy; and (*e–h*) the added in-plane Reynolds shear stress.

time-averaged wake width on the inflow turbulence intensity can be found in the literature e.g. $k = 0.38\mathrm{TI} + 0.004$ proposed by Niayifar & Porté-Agel (2016). However, to the best of the authors' knowledge, similar empirical formulae for σ_{y_c} and $\sigma_{r_{1/2}}$ do not exist yet, which need further investigation.

5.3. *Relation between the time-averaged wake and the instantaneous wake*

This section is dedicated to relating the time-averaged wake and the instantaneous wake to the standard deviation of the wake centre position σ_{y_c}, which represents the wake meandering amplitude.

To derive the relations, hypotheses are made as follows. At any downstream location x,

(i) the wake centre position y_c follows the normal distribution $\mathcal{N}(\overline{y_c}, \sigma_{y_c}^2)$, i.e. the probability function of the wake centre is

$$\mathcal{P}(y_c = \xi) = \frac{1}{\sqrt{2\pi}\sigma_{y_c}} \exp\left(-\frac{(\xi - \overline{y_c})^2}{2\sigma_{y_c}^2}\right), \tag{5.1}$$

as shown in figure 17;

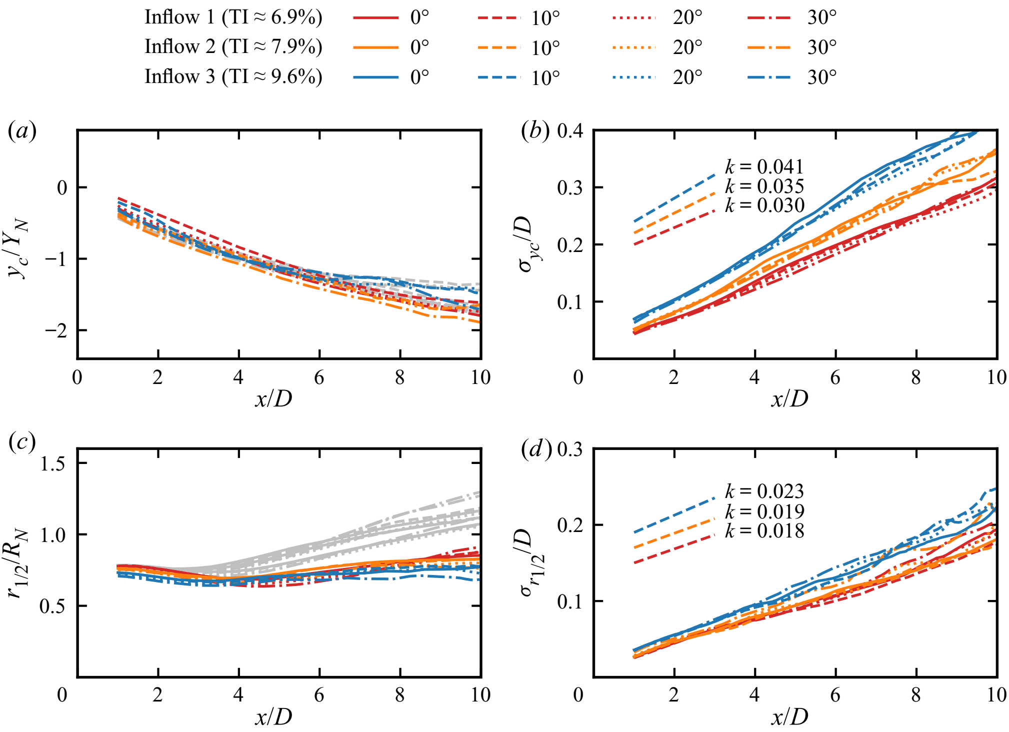

Figure 23. Effects of inflow turbulence on the instantaneous wake quantities: (*a*) the mean of the instantaneous wake centre positions y_c; (*b*) the standard deviation of the instantaneous wake centre position σ_{y_c}; (*c*) the mean of the characteristic instantaneous wake width $r_{1/2}$; and (*d*) the standard deviation of the characteristic instantaneous wake width $\sigma_{r_{1/2}}$. In (*a*,*c*), the curves in grey scale plot the corresponding terms obtained from the time-averaged wake. In (*b*,*d*), the growth rates k of σ_{y_c} and $\sigma_{r_{1/2}}$ are illustrated by a short dashed line for each inflow condition.

(ii) the transverse profiles of instantaneous velocity deficits can be approximated by a Gaussian function with $\Delta u(y,\xi) = \Delta u_c \exp(-((y-\xi)^2/2s^2))$ as shown in figure 16, where s is the standard deviation of the Gaussian function related to the wake width with $r_{1/2} = \sqrt{2\ln 2}s$ and ξ is the instantaneous wake centre.

The time-averaged velocity deficit ΔU can be regarded as the ensemble-average of the instantaneous velocity deficits, so it can be calculated by multiplying the p.d.f. of the wake centre $P(y_c = \xi)$ with the instantaneous wake deficit function $\Delta u(y,\xi)$ and integrating ξ from $-\infty$ to $+\infty$, as follows,

$$\begin{aligned}\Delta U(y) &= \int_{-\infty}^{+\infty} \mathcal{P}(y_c = \xi)\Delta u(y,\xi)\,\mathrm{d}\xi \\ &= \int_{-\infty}^{+\infty} \frac{1}{\sqrt{2\pi}\sigma_{y_c}} \exp\left(-\frac{(\xi-\overline{y_c})^2}{2\sigma_{y_c}^2}\right)\Delta u_c \exp\left(-\frac{(y-\xi)^2}{2s^2}\right)\mathrm{d}\xi \\ &= \sqrt{\frac{s^2}{\sigma_{y_c}^2+s^2}}\Delta u_c \exp\left(\frac{(y-\overline{y_c})^2}{2(\sigma_{y_c}^2+s^2)}\right). \qquad (5.2)\end{aligned}$$

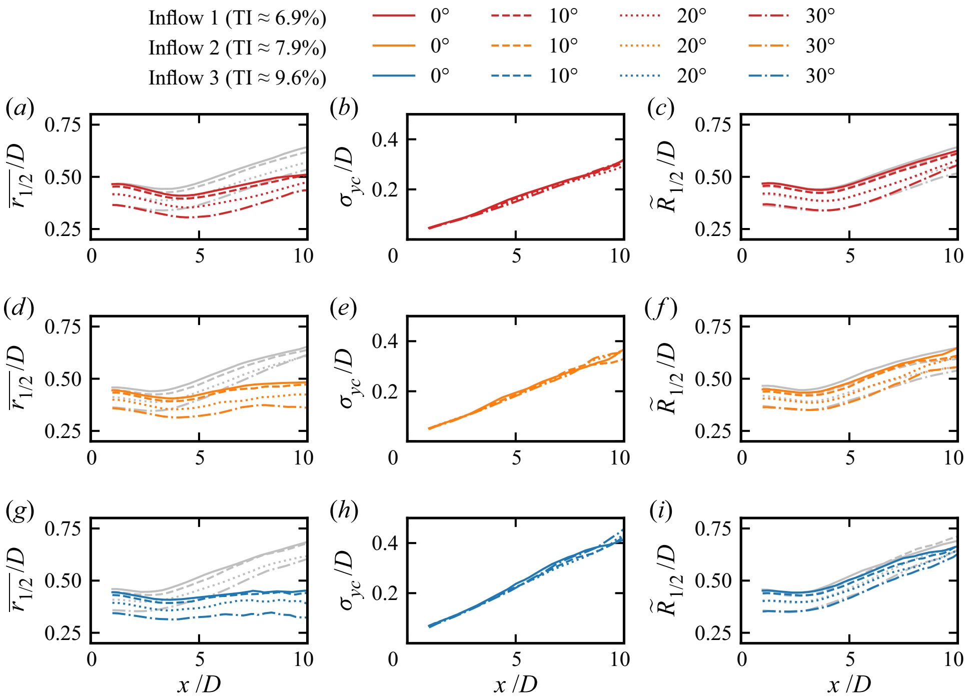

Figure 24. (a,d,g) Mean of the instantaneous wake width $\overline{r_{1/2}}$ (in colour) compared with the time-averaged wake width $R_{1/2}$ (in grey). (b,e,h) Standard deviation of the wake centre position. (c,f,i) The predicted time-averaged wake width $\tilde{R}_{1/2}(x) = \sqrt{2\ln 2\sigma_{y_c}^2(x) + \overline{r_{1/2}(x)}^2}$ (in colour) compared with the time-averaged simulation results $R_{1/2}$ (in grey).

Comparing (5.2) and (3.3), one obtains the following relations,

$$\Delta U_C = \sqrt{\frac{s^2}{\sigma_{y_c}^2 + s^2}}\Delta u_c, \tag{5.3}$$

$$S = \sqrt{\sigma_{y_c}^2 + s^2}. \tag{5.4}$$

Recall the definition of the wake width is $R_{1/2} = \sqrt{2\ln 2}S$ and $\overline{r_{1/2}} = \sqrt{2\ln 2}s$ for the time-averaged and instantaneous wakes, respectively. One obtains the relation of $R_{1/2}$, $\overline{r_{1/2}}$ and σ_{y_c} as

$$R_{1/2}(x) = \sqrt{2\ln 2\,\sigma_{y_c}^2(x) + \overline{r_{1/2}(x)}^2}. \tag{5.5}$$

This relation is validated with the simulation results for all the inflow conditions and yaw angles in figures 24 and 25. Figure 24 compares the wake width predicted by (5.5) with that from simulation. The panels (a,d,g) show clearly the difference between the instantaneous wake width (in colour) and the time-averaged wake width (in grey), whereas the panels (c,f,i) show an excellent agreement between the time-averaged wake width calculated by (5.5) (in colour) and the simulation results (in grey). Figure 25 compares the mean of the instantaneous centreline velocity deficit Δu_c with the time-averaged centreline velocity deficit ΔU_C. The panels (a,d,g) show that the discrepancies between these two definitions increase with downstream distance owing to the increasing wake meandering amplitudes

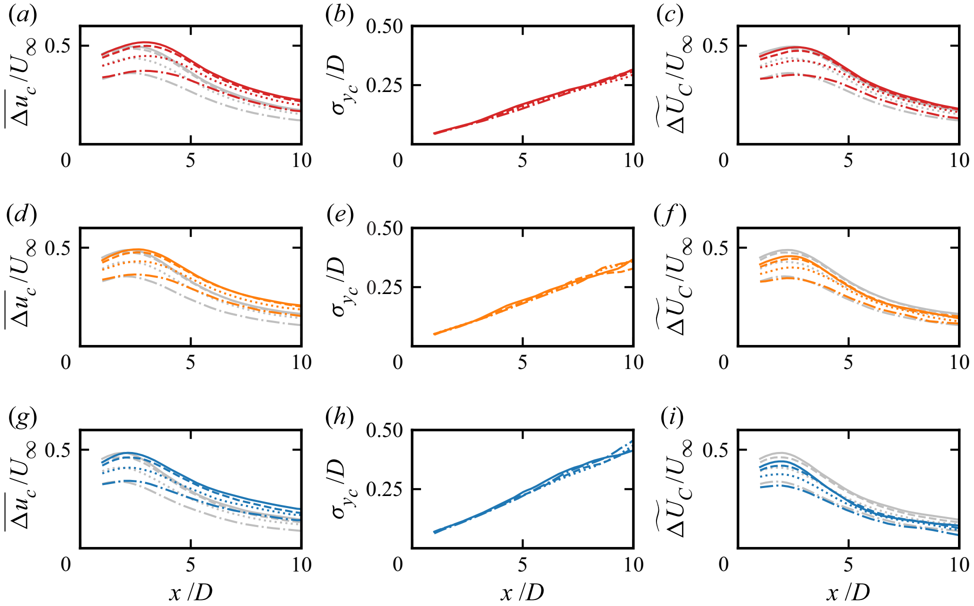

Figure 25. (*a*,*d*,*g*) Mean of the instantaneous velocity deficit $\overline{\Delta u_c}$ (in colour) compared with the time-averaged wake velocity deficit ΔU_C (in grey). (*b*,*e*,*h*) Standard deviation of the wake centre position. (*c*,*f*,*i*) The predicted time-averaged velocity deficit $\tilde{\Delta U_C}(x) = \sqrt{s^2/(s^2+\sigma_{y_c}^2)}$ (in colour) compared with the simulation results U_C (in grey). See figure 24 for the legend.

in the far wake, as shown in panels (*b*,*e*,*h*). In panels (*c*,*f*,*i*), the prediction $\tilde{\Delta U_C}$ using (5.3) agrees well with the computed ΔU_C from the time-averaged simulation results. This agreement shows that the contribution of the wake meandering can be well captured by (5.3).

Physically speaking, the derived relations and observations in figures 24 and 25 show the relative importance of (i) wake meandering and (ii) turbulence diffusion and pressure (on the moving frame of reference located at the instantaneous wake centre) on the recovery of the wake, i.e. the decrease of velocity deficit and the growth of wake radius. When the wake meandering amplitude is small ($\sigma_{y_c} < r_{1/2}$) in the near wake, the recovery of the time-averaged wake is dominated by the second factor mentioned above. Otherwise, when the meandering amplitude is large ($\sigma_{y_c} > r_{1/2}$), the recovery of the time-averaged wake is mainly caused by the wake meandering. Additionally, because σ_{y_c} is independent of yaw angle, this equation explains why the far-wake width, where the inflow turbulence is dominant, is poorly scaled with R_N (derived based on the turbine operation condition for the near wake). These findings and the derived relations can be employed in the development of advanced wake meandering models to take into account more accurately the instantaneous wake features instead of using models based on the time-averaged wake (Jiménez *et al.* 2010; Bastankhah & Porté-Agel 2016; Shapiro *et al.* 2018).

6. Summary and conclusion

We investigate the wake characteristics of a yawed utility-scaled wind turbine using LES with the blades and nacelle parametrized using the actuator surface model. Four yaw angles ($\gamma = 0^\circ$, 10°, 20°, 30°) are considered with the turbine operating at three modified

TSRs ($\tilde{\lambda} = 7, 8, 9$) defined based on the velocity projected to the axial direction of the rotor. For TSR $\tilde{\lambda} = 8$, we further investigate the effects of three different turbulent inflows on the wake dynamics of turbines with different yaw angles.

Similarities between cases with different yaw angles are observed for different characteristics of turbine wakes under different turbine operation conditions. For the time-averaged flow field, we examine two kinds of similarities, i.e. the similarity of the streamwise velocity deficit and the similarity of the transverse velocity. It is observed that the wake deficits ΔU of cases with different yaw angles overlap well with each other when normalized using the characteristic velocity U_N, i.e. the velocity difference between the incoming velocity and velocity in the near wake of the turbine, and the characteristic length R_N, i.e. the radius of the near wake, which are derived from the one-dimensional momentum theory. For the transverse motion of the wake, the transverse deflection Y_C and the magnitude of the transverse velocity V are observed to scale well with the length scale Y_N and the velocity scale V_N, respectively, which are derived using the transverse component of the thrust on the turbine. The width $R^V_{1/2}$ of the region dominated by the transverse velocity, on the other hand, is similar for cases of different yaw angles and scales well by the rotor diameter. For the turbulence characteristics of the wake, the computed results show a good scaling of the turbine-added turbulence kinetic energy Δk and the Reynolds shear stress $\Delta\langle u'v'\rangle$ at far-wake locations when normalized by U_T, which is defined using the streamwise component of the thrust on the turbine. For the statistics of the instantaneous wake, the p.d.f. profiles of the instantaneous wake positions y_c normalized using rotor diameter are observed to overlap with each other for cases of different yaw angles. Meanwhile, we find that the standard deviation of the instantaneous wake deflection fluctuations σ_{y_c} and of the instantaneous wake radius fluctuations $\sigma_{r_{1/2}}$ overlap with each other when normalized using the incoming velocity and rotor diameter without using the characteristic scales depending on yaw angles. We further examine the above-mentioned wake characteristics for different inflows. Similarities are in general observed for cases of different yaw angles under the same inflow. When comparing results from different inflows, some quantities, e.g. the standard deviation of the position of instantaneous wake centres and the standard deviation of the radius of instantaneous wakes, are observed as being affected by the inflow turbulence. Two more interesting observations are: (i) the mean of the instantaneous wake width $\overline{r_{1/2}}$, which barely grows travelling downstream, is smaller than the time-averaged wake width $R_{1/2}$; (ii) the mean of the velocity deficit located at the instantaneous centreline $\overline{\Delta u_c}$ recovers slower than the time-averaged centreline velocity deficit ΔU_C. By assuming normal distribution for the positions of instantaneous wake centres, two analytical expressions are then proposed to relate the mean of the instantaneous wake quantities averaged on the frame of reference following instantaneous wake centres, i.e. $\overline{r_{1/2}}$ and $\overline{\Delta u_c}$, with those of the time-averaged wake with the wake meandering amplitude. Overall, we have observed that the characteristics of time-averaged wake, which include ΔU, $R_{1/2}$, Y_C and V except for $R^V_{1/2}$, scale well using the velocity and length scales defined based on turbine operational conditions, while the characteristics of wake fluctuations, which include p.d.f. (y_c), σ_{y_c} and $\sigma_{r_{1/2}}$, are independent of yaw angles and TSRs. This suggests that the yaw of a turbine mainly influences the time-averaged wake characteristics, while the characteristics of wake fluctuations are largely affected by the incoming turbulence for the considered cases.

The similarity observed on the time-averaged flow fields suggests that the wake behind a yawed wind turbine can be decomposed into a straight wake behind an equivalent non-yawed wind turbine and a deflected centreline caused by the transverse component of the thrust on the turbine, which is also the assumption for deriving the corresponding velocity and length scales. Furthermore, the simulation results show that the transverse motion and the streamwise velocity deficit of the wake reside in different regions with different influencing zones, the wake width defined based on the streamwise velocity deficit $R_{1/2}$ decreases when increasing the yaw angle γ, and the width defined based on the transverse velocity $R^V_{1/2}$ barely changes with the yaw angle. A note here is that the fitting method employed for the transverse velocity can introduce uncertainty to the value of $R^V_{1/2}$, as shown in Appendix E. The present results suggest that the employed CVP fitting performs better than Gaussian fitting for the transverse velocity. The decomposition of the wake into streamwise and transverse components can potentially be employed to simplify the development of analytical models. The differences between the transverse velocity and the streamwise velocity deficit, on the other hand, make it difficult to predict quantities related to the wake's transverse motion with analytical models based on the momentum theory, and these needs to be considered to improve the existing analytical models (Jiménez *et al.* 2010; Bastankhah & Porté-Agel 2016; Qian & Ishihara 2018). The similarity observed in this work provides a new way to model the transverse motion of the wake from a yawed wind turbine where the wake deflection, transverse velocity and other quantities can be computed using the simulation results at one yaw angle together with the velocity and length scales employed in this work.

To conclude, the observed various similarity characteristics for different turbulence statistics show a potential for the decoupling between the meandering motion of the wake and the turbine-added wake turbulence. That the p.d.f. (y_c), σ_{y_c} and $\sigma_{r_{1/2}}$ scaled by D suggests that wake meandering is mainly dominated by the incoming large eddies instead of the turbine operational conditions. The turbine-added turbulence kinetic energy can be decomposed into two parts, i.e. the part caused by the shear layer in the wake and the nominal part caused by the meandering motion of the wake. The meandering motion is similar for the same inflow, such that the overlap of the Δk profile, when scaled by U_T, implies its similarity on the coordinate system following the meandering motion of the wake. This suggests an efficient approach to develop advanced models for wake dynamics, where the wake turbulence and the meandering motion can be modelled separately. However, further work has to be carried out to develop such models. One problem is how to model the effects of meandering motion on wake turbulence in the coordinate system following the meandering motion of the wake. To solve this problem, one approach is to treat the velocity deficit and wake turbulence as passive scales, as done in the dynamic wake meandering model developed at Technical University of Denmark (Larsen *et al.* 2007). In the dynamic wake meandering model, the wake radius and velocity deficit have to be modelled on the moving frame of reference following the wake centre. The relations proposed in this work ((5.2) and (5.5)) indicate that the wake radius and velocity deficit can be estimated using those of the time-averaged wake and the standard deviation of the wake centre fluctuations, for which the latter can be approximated based on Taylor's frozen flow hypothesis or advanced models for space–time correlations (He, Jin & Yang 2017; Yang 2020). The other problem is how to account for the bluff body shear layer instability on the meandering motion of turbine wakes (Heisel, Hong & Guala 2018; Yang & Sotiropoulos 2019*a*), which often happens at higher frequency (Yang & Sotiropoulos 2019*b*) and has been shown to play an important role in the wake of utility-scale wind turbines (Foti *et al.* 2018) and wind farms (Foti *et al.* 2019). Moreover, how incoming

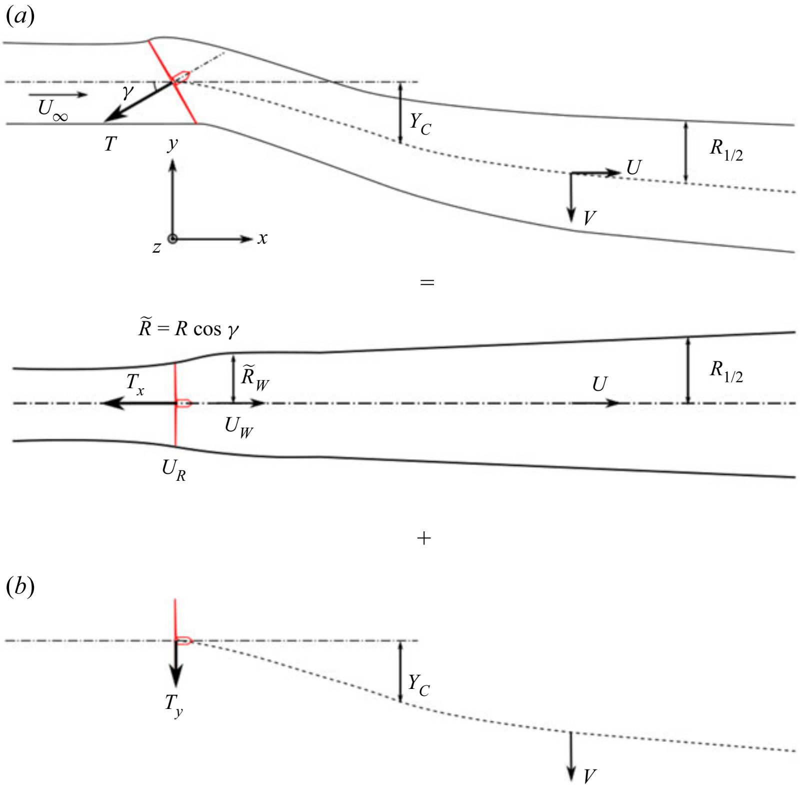

Figure 26. Decomposition of the wake behind a yawed wind turbine into: (*a*) an equivalent non-yawed wind turbine's wake of streamwise thrust T_x; and (*b*) the wake transverse velocity and the centreline deflection caused by the transverse thrust component T_y.

turbulence and stratification conditions affect the similarity observed in this work need to be further investigated in the future.

Funding. This work is partially supported by NSFC Basic Science Center Program for 'Multiscale Problems in Nonlinear Mechanics' (NO. 11988102).

Declaration of interests. The authors report no conflict of interest.

Author ORCIDs.
Zhaobin Li https://orcid.org/0000-0003-2224-7074;
Xiaolei Yang https://orcid.org/0000-0002-2606-0672.

Appendix A. Derivation of velocity scales and length scales for yawed turbine wakes

In this appendix we derive the velocity and length scales for yawed turbine wakes based on one-dimensional momentum theory. We assume that the streamwise velocity U and the spanwise velocity V are independent and the wake can be decomposed into a straight wake generated by an equivalent non-yawed turbine and wake deflection owing to the yaw of the turbine, as illustrated in figure 26.

First, we derive the characteristic velocity U_N and characteristic length R_N by applying one-dimensional momentum theory to the equivalent non-yawed turbine. The equivalent non-yawed turbine is defined as a turbine of thrust T_x, the same as the streamwise component of the yawed turbine, and an elliptical rotor-swept area with the horizontal radius being $\tilde{R} = R\cos\gamma$ and the vertical radius being R and computed as

$$\tilde{A} = \pi\tilde{R}R = \pi R^2 \cos\gamma = A\cos\gamma \tag{A1}$$

with A as the rotor sweeping area. With the thrust component aligned with the inflow computed as $T_x = T\cos\gamma$, the thrust coefficient of this equivalent turbine is defined as follows:

$$C_{T_x} = \frac{T_x}{\frac{1}{2}\tilde{A}\rho U_\infty^2} = \frac{T\cos\gamma}{\frac{1}{2}A\cos\gamma\rho U_\infty^2} = \frac{T}{\frac{1}{2}A\rho U_\infty^2}. \tag{A2}$$

Substituting (3.1) into (A2) yields

$$C_{T_x} = \tilde{C}_T \cos^2\gamma. \tag{A3}$$

Based on the one-dimensional momentum theory (Burton *et al.* 2011), the streamwise velocity U_W in the turbine's near wake is obtained as follows:

$$U_W = U_\infty\sqrt{1 - C_{T_x}} = U_\infty\sqrt{1 - \tilde{C}_T\cos^2\gamma}. \tag{A4}$$

Then, U_N is obtained as the different between the inflow velocity U_∞ and the wake velocity U, as in (3.5), as follows:

$$U_N = U_\infty - U_W = U_\infty\left(1 - \sqrt{1 - \tilde{C}_T\cos^2\gamma}\right), \tag{A5}$$

which is the streamwise velocity deficit in the near wake of the equivalent non-yawed wind turbine. This expression is the same as that in the wake model of Shapiro *et al.* (2018) for the initial streamwise velocity deficit.

The length scale for the wake width R_N is defined as the width of the imminent wake of the equivalent non-yawed wind turbine, which reflects the expansion of the streamtube encompassing the rotor owing to the flow deceleration and can be computed from the mass conservation equation. To derive R_N, we first compute the streamwise velocity at the rotor disc, as

$$U_R = \tfrac{1}{2}(U_\infty + U_W) = \tfrac{1}{2}U_\infty\left(1 + \sqrt{1 - \tilde{C}_T\cos^2\gamma}\right). \tag{A6}$$

Following Bastankhah & Porté-Agel (2016), the wake cross-section normal to the streamwise direction is also assumed to be elliptical, with transverse radius $\tilde{R}_W = R_W\cos\gamma$, where R_W is the vertical wake radius. Based on the conservation of mass rate in the streamtube, we obtain

$$\dot{m} = \rho\pi\tilde{R}RU_R = \rho\pi\tilde{R}_W R_W U_W, \tag{A7}$$

which gives the final expression for R_N as

$$R_N \doteq \tilde{R}_W = R\cos\gamma\sqrt{\frac{1 + \sqrt{1 - \tilde{C}_T\cos^2\gamma}}{2\sqrt{1 - \tilde{C}_T\cos^2\gamma}}}. \tag{A8}$$

We then derive the velocity scale V_N and length scale Y_N for the wake deflection arising from the yaw of the turbine. The velocity scale V_N for the transverse motion of the wake can be derived with the spanwise momentum theory as follows:

$$V_N = \frac{T_y}{\rho A U_\infty} = \frac{\frac{1}{2}\rho A \tilde{C}_T \cos^2\gamma \sin\gamma\, U_\infty^2}{\rho A U_\infty} = \frac{1}{2} U_\infty \tilde{C}_T \cos^2\gamma \sin\gamma. \tag{A9}$$

It is worth noting that the denominator is computed with A, instead of the projected area $A\cos\gamma$, to reflect the fact that the width of the spanwise velocity $R_{1/2}^V$ is constant for different yaw angles. The resulting V_N is the same as that of Jiménez *et al.* (2010) for the initial transverse velocity, and is twice as large as the initial transverse velocity in the model of Shapiro *et al.* (2018).

The length scale for the wake centre location Y_N is obtained by multiplying V_N by a typical time scale D/U_∞ and is shown as

$$Y_N = D\tilde{C}_T \cos^2\gamma \sin\gamma. \tag{A10}$$

The velocity scale for the turbine-added turbulence is obtained following Yang *et al.* (2015*a*) and Foti *et al.* (2018), where a velocity scale U_T is defined with the thrust force T and the rotor area A for non-yawed wind turbines, as follows:

$$U_T = \sqrt{\frac{T}{\rho A}}. \tag{A11}$$

By substituting (3.1) into (A11), the corresponding U_T for yawed wind turbines is obtained as follows:

$$U_T = \sqrt{\rho A \frac{\tilde{C}_T \cos^2\gamma\, U_\infty^2}{2\rho A}} = U_\infty \cos\gamma \sqrt{\frac{\tilde{C}_T}{2}}. \tag{A12}$$

Figure 27 compares the proposed velocity and length scales, which vary with the thrust coefficients yaw angle γ for different thrust coefficients $\tilde{C}_T$.

Appendix B. Wake width in the study of Bastankhah & Porté-Agel (2016)

In (6.10) of the paper by Bastankhah & Porté-Agel (2016), an analytical expression of wake width is represented with the standard variation of a Gaussian curve fit as follows (adapted with the present nomenclature),

$$\frac{S}{R} = \cos\gamma \sqrt{\frac{1+\sqrt{1-\tilde{C}_T\cos^3\gamma}}{2\left(1+\sqrt{1-\tilde{C}_T\cos^2\gamma}\right)}} \approx \cos\gamma\sqrt{\frac{1}{2}} \tag{B1}$$

assuming small γ. Here, (A8) and (B1) are different because Bastankhah & Porté-Agel (2016) employed a different way to calculate the rotor induction factor with C_T, which resulted in a different flow velocity at the rotor.

Appendix C. Influence of spatial and temporal resolutions

In this appendix, a brief study of the effect of spatial and temporal resolution on the simulation results is presented. Three cases of different grid sizes and time steps (as shown in table 4) are investigated, where the medium case corresponds to the resolution employed

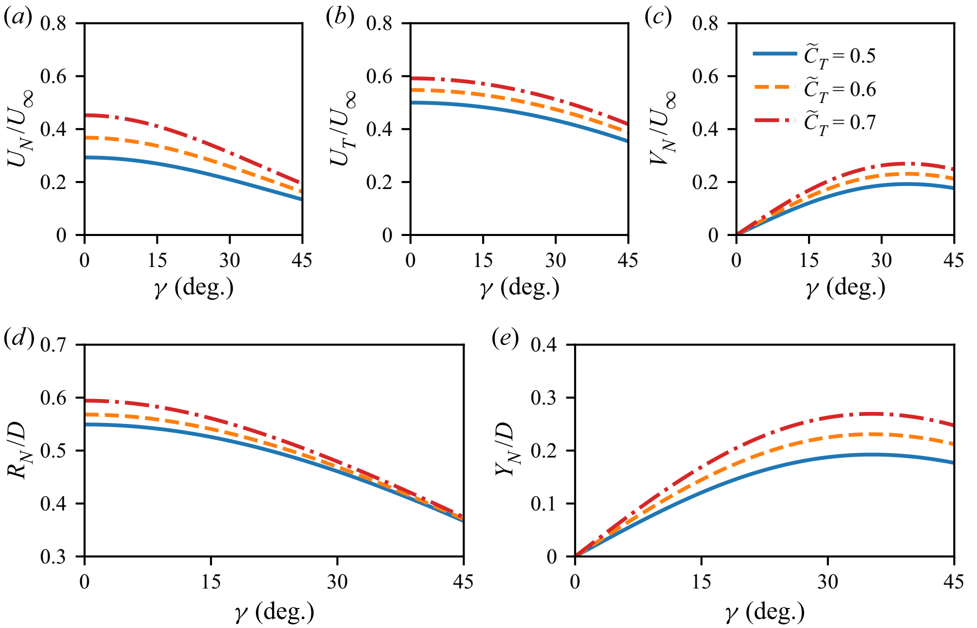

Figure 27. The proposed velocity and length scales varying with yaw angle γ for different thrust coefficients $\tilde{C}_T$.

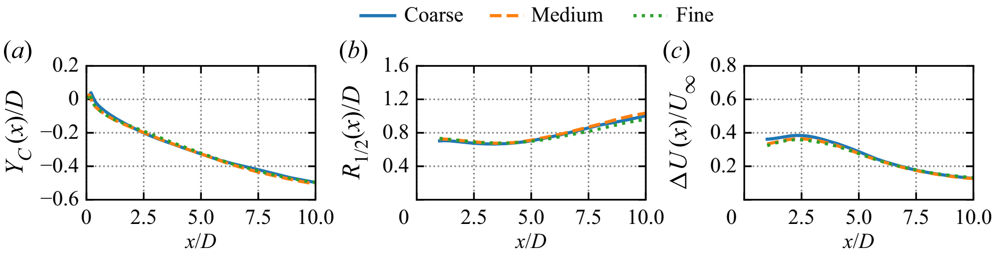

Figure 28. Effect of spatial and temporal resolution on the time-averaged results of: (*a*) wake centreline deflection $Y_C(x)$; (*b*) the wake width $R_{1/2}(x)$; and (*c*) the characteristic velocity deficit.

in the present work. The grid sizes in three directions are changed simultaneously with the size of time steps changed accordingly to keep the Courant–Friedrichs–Lewy (CFL) number constant. In all the cases listed in table 4, $\tilde{\lambda} = 8$ and $\gamma = 30^\circ$. Figures 28 and 29 show the influence of the resolution on the time-averaged wake characteristics. It is found that the wake centreline, the wake width and the characteristic velocity deficit remain almost the same with mesh refinement, as shown in figure 28. The differences between different resolutions are also observed as being minor for the profiles of the time-averaged velocity deficit and the turbine-added TKE at different turbine downstream locations, as shown in figure 29.

Appendix D. Influence of yaw direction on wake characteristics

In this section, we briefly investigate the influence of the direction of yaw misalignment. Previous studies (Fleming *et al.* 2014; Bastankhah & Porté-Agel 2016; Gebraad *et al.* 2017)

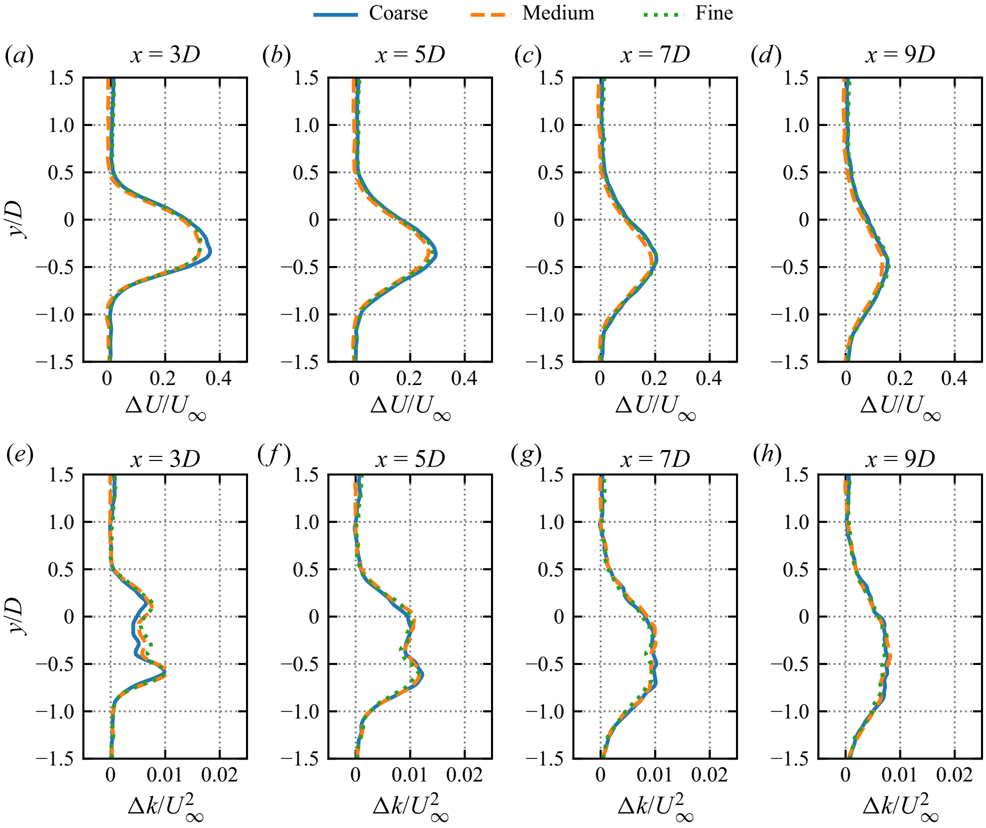

Figure 29. Effect of the spatial and the temporal resolutions on the profiles of: (*a*–*d*) the velocity deficit; and (*e*–*h*) the turbine-added turbulence kinetic energy.

	Δx	$\Delta y = \Delta z$	Δt
Coarse	$D/15$	$D/30$	$0.0135D/U_\infty$
Medium	$D/20$	$D/40$	$0.0180D/U_\infty$
Fine	$D/25$	$D/50$	$0.0225D/U_\infty$

Table 4. Spatial and temporal resolution employed for the convergence study.

suggested that the centreline of the wake behind a non-yawed wind turbine may be deflected to one side owing to the rotation in the wake caused by the rotation of turbine's blades and the incoming flow. To examine the effect of rotor rotation on the wake of yawed wind turbines, we conducted an extra simulation with negative yaw angle, i.e. $\gamma = -30^\circ$, for the case with $\tilde{\lambda} = 8$ and inflow 1.

Simulation results of $\gamma = 30^\circ$ and $\gamma = -30^\circ$ are compared in figure 30 for different quantities of the wake. Figure 30(*a*) compares the wake centreline deflection for $\gamma = \pm 30^\circ$. To facilitate the comparison, the wake centreline of $\gamma = -30^\circ$ is reflected with respect to $y = 0$ and is plotted in grey. A generally good agreement between the two lines was found. The deflection of $\gamma = 30^\circ$ was slightly larger in the far wake,

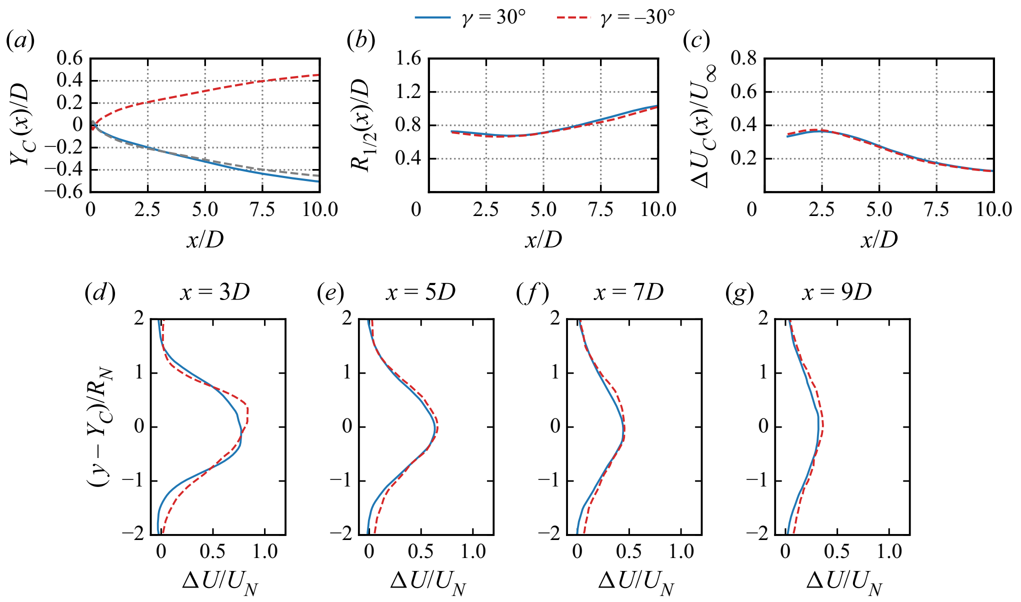

Figure 30. Wake characteristics with negative and positive yaw angles for: (*a*) the wake centerline, the grey dashed lines shows the reflected wake centreline of $\gamma = -30°$ for comparison; (*b*) the wake width; (*c*) the wake centre velocity deficit; and (*d–g*) the transverse profiles of the velocity deficit.

because in the non-yawed case, the wake centreline was slightly skewed towards $-y$ (see figure 6). The wake width $R_{1/2}$ and the characteristic velocity deficit ΔU_C agreed well for the two opposite yaw angles, as shown in figure 30(*b*,*c*). In figure 30(*d*–*g*), the horizontal profiles of the velocity deficit are shown. At $x = 3D$, discrepancies are observed between the two profiles, where the velocity deficit profiles are not symmetric. On the other hand, the wake profiles agree well with each other for $x > 5D$.

Appendix E. Fitting of the transverse velocity

In this appendix, we explain how the transverse velocity is fitted to extract its features. According to Howland *et al.* (2016) and Bastankhah & Porté-Agel (2016), the transverse velocity in the wake of a yawed wind turbine is induced by a pair of counter-rotating vortices, as illustrated in figure 31(*a*). For simplicity, the influences of the wake rotation and the ground are not considered, and the vortices are assumed as being symmetric with respect to the hub-height plane. Each vortex has a circulation magnitude of Γ and is located $H(x)$ from the hub-height plane. The induced transverse velocity at the hub height can be calculated using the Biot–Savart law as follows,

$$V(x, y) = \frac{\Gamma(x)}{\pi L}\cos\theta, \tag{E1}$$

with $L = \sqrt{H^2(x) + (y - Y_C^V(x))^2}$ as the distance to the vortex centre, $\cos\theta = H(x)/L$ and $Y_C^V(x)$ is the centreline position of the transverse velocity V. At each downstream location x, the lateral profile of the transverse velocity $V(x, y)$ at the hub height is substituted into (E1) together with the transverse coordinate y to obtain $\Gamma(x)$, $H(x)$ and $Y_C^V(x)$ using the method of least squares. It is found that the so-computed function fits well

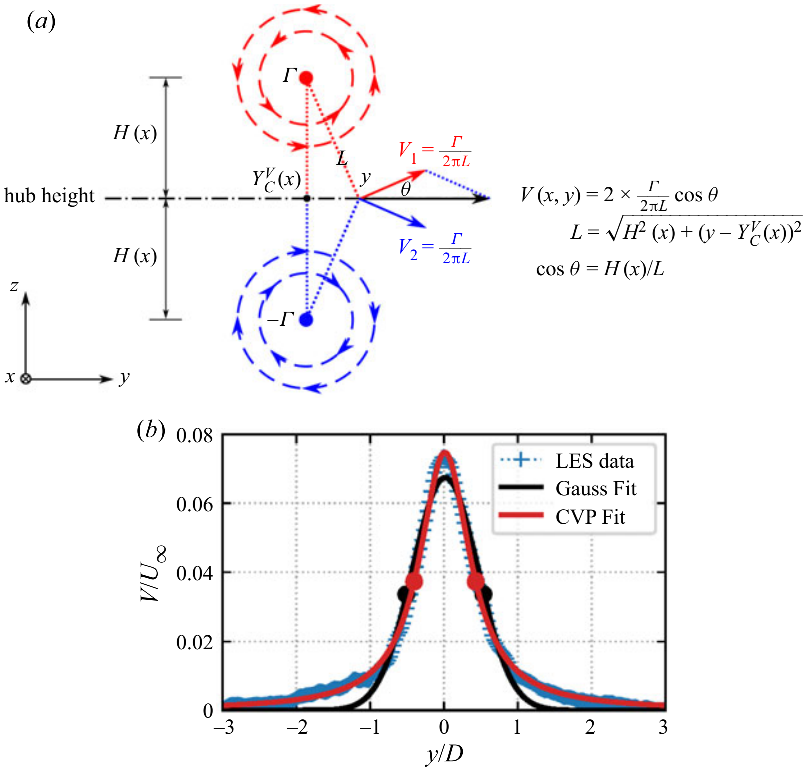

Figure 31. (*a*) Schematic on computing the transverse velocity (V) at hub height induced by a CVP, and (*b*) the fitting of the V profile to CVP and Gaussian functions for the case with $\gamma = 30^\circ$, $\tilde{\lambda} = 8$ at downstream location $x/D = 6$. The solid dots indicate the halfwidth of the wake defined by each fitting method.

to the transverse profile of V, as shown in figure 12(*e*–*h*). Once the fitting parameters are determined, the characteristic transverse velocity $V_C(x)$ is computed as the peak transverse velocity (at $y = Y_C^V(x)$), i.e.

$$V_C(x) = \frac{\Gamma(x)}{\pi H(x)}, \tag{E2}$$

and the half-width of the transverse velocity $R_{1/2}^V(x)$ is defined as the position where the transverse velocity is reduced to half of the peak value, as

$$V(x, Y_C^V(x) \pm R_{1/2}^V(x)) = \tfrac{1}{2} V_C(x). \tag{E3}$$

Substituting (E1) and (E2) into (E3) results in

$$R_{1/2}^V(x) = H(x). \tag{E4}$$

The CVP fitting is compared with the Gaussian fitting in figure 31(*b*). It is observed that the physics-based CVP fitting can capture well the variation of the transverse velocity V in the spanwise direction y. The Gaussian function, on the other hand, fails to capture the peak and the halfwidth of the distribution of the transverse velocity. This comparison shows the importance of choosing proper fitting functions for extracting wake features from simulation results. Different fitting functions should be employed for different wake quantities. The results obtained from this work reveal that the Gaussian shape is still proper to approximate the streamwise velocity deficit even with yaw angles. However, the transverse velocity is non-Gaussian even in the far wake and the physics-based CVP fitting can be employed to obtain correct wake features.

REFERENCES

ABKAR, M. & PORTÉ-AGEL, F. 2015 Influence of atmospheric stability on wind-turbine wakes: a large-eddy simulation study. *Phys. Fluids* **27** (3), 035104.

AINSLIE, J.F. 1988 Calculating the flowfield in the wake of wind turbines. *J. Wind Engng Ind. Aerodyn.* **27** (1–3), 213–224.

ANNONI, J., GEBRAAD, P.M.O., SCHOLBROCK, A.K., FLEMING, P.A. & VAN WINGERDEN, J.-W. 2016 Analysis of axial-induction-based wind plant control using an engineering and a high-order wind plant model. *Wind Energy* **19** (6), 1135–1150.

BARTHELMIE, R.J., *et al.* 2009 Modelling and measuring flow and wind turbine wakes in large wind farms offshore. *Wind Energy* **12** (5), 431–444.

BARTL, J., MÜHLE, F., SCHOTTLER, J., SÆTRAN, L., PEINKE, J., ADARAMOLA, M. & HÖLLING, M. 2018 Wind tunnel experiments on wind turbine wakes in yaw: effects of inflow turbulence and shear. *Wind Energy Sci.* **3** (1), 329–343.

BASTANKHAH, M. & PORTÉ-AGEL, F. 2014 A new analytical model for wind-turbine wakes. *Renewable Energy* **70**, 116–123.

BASTANKHAH, M. & PORTÉ-AGEL, F. 2016 Experimental and theoretical study of wind turbine wakes in yawed conditions. *J. Fluid Mech.* **806**, 506–541.

BASTANKHAH, M. & PORTÉ-AGEL, F. 2017 Wind tunnel study of the wind turbine interaction with a boundary-layer flow: upwind region, turbine performance, and wake region. *Phys. Fluids* **29** (6), 65105.

BASTANKHAH, M. & PORTÉ-AGEL, F. 2019 Wind farm power optimization via yaw angle control : a wind tunnel study. *J. Renew. Sustain. Energy* **11** (2), 23301.

BLOCKEN, B., STATHOPOULOS, T. & CARMELIET, J. 2007 CFD simulation of the atmospheric boundary layer: wall function problems. *Atmos. Environ.* **41** (2), 238–252.

BRUNTON, S.L., NOACK, B.R. & KOUMOUTSAKOS, P. 2020 Machine learning for fluid mechanics. *Annu. Rev. Fluid Mech.* **52**, 477–508.

BURTON, T., JENKINS, N., SHARPE, D. & BOSSANYI, E. 2011 *Wind Energy Handbook*. John Wiley & Sons.

CALVERT, J.R. 1967 Experiments on the flow past an inclined disk. *J. Fluid Mech.* **29** (4), 691–703.

CHAMORRO, L.P., LEE, S.-J., OLSEN, D., MILLIREN, C., MARR, J., ARNDT, R.E.A. & SOTIROPOULOS, F. 2015 Turbulence effects on a full-scale 2.5 MW horizontal-axis wind turbine under neutrally stratified conditions. *Wind Energy* **18** (2), 339–349.

CHATTOT, J. 2014 Actuator disk theory-steady and unsteady models. *Trans. ASME: J. Solar Energy Engng* **136** (3), 031012.

CRAMER, D. 2002 *Basic Statistics for Social Research: Step-by-Step Calculations & Computer Techniques using Minitab*. Routledge.

CRESPO, A. & HERNA, J. 1996 Turbulence characteristics in wind-turbine wakes. *J. Wind Engng Ind. Aerodyn.* **61** (1), 71–85.

DU, Z. & SELIG, M. 1998 A 3-D stall-delay model for horizontal axis wind turbine performance prediction. In *1998 ASME Wind Energy Symposium*, 1998-21, AIAA.

DURAISAMY, K., IACCARINO, G. & XIAO, H. 2019 Turbulence modeling in the age of data. *Annu. Rev. Fluid Mech.* **51**, 357–377.

FLEMING, P.A., GEBRAAD, P.M.O., LEE, S., VAN WINGERDEN, J.W., JOHNSON, K., CHURCHFIELD, M., MICHALAKES, J., SPALART, P. & MORIARTY, P. 2014 Evaluating techniques for redirecting turbine wakes using SOWFA. *Renew. Energy* **70**, 211–218.

FOTI, D., YANG, X., SHEN, L. & SOTIROPOULOS, F. 2019 Effect of wind turbine nacelle on turbine wake dynamics in large wind farms. *J. Fluid Mech.* **869**, 1–26.

FOTI, D., YANG, X. & SOTIROPOULOS, F. 2018 Similarity of wake meandering for different wind turbine designs for different scales. *J. Fluid Mech.* **842**, 5–25.

FUERTES, F., MARKFORT, C. & PORTÉ-AGEL, F. 2018 Wind turbine wake characterization with nacelle-mounted wind Lidars for analytical wake model validation. *Remote Sens.* **10** (5), 668.

GAO, S., TAO, L., TIAN, X. & YANG, J. 2018 Flow around an inclined circular disk. *J. Fluid Mech.* **851**, 687–714.

GE, L. & SOTIROPOULOS, F. 2007 A numerical method for solving the 3D unsteady incompressible Navier–Stokes equations in curvilinear domains with complex immersed boundaries. *J. Comput. Phys.* **225** (2), 1782–1809.

GEBRAAD, P., THOMAS, J.J., NING, A., FLEMING, P. & DYKES, K. 2017 Maximization of the annual energy production of wind power plants by optimization of layout and yaw-based wake control. *Wind Energy* **20** (1), 97–107.

GERMANO, M., PIOMELLI, U., MOIN, P. & CABOT, W.H. 1991 A dynamic subgrid-scale eddy viscosity model. *Phys. Fluids* A **3** (7), 1760–1765.

GLAUERT, H. 1926 A general theory of the autogyro. *Tech. Rep.* HM Stationery Office.

HE, G., JIN, G. & YANG, Y. 2017 Space-time correlations and dynamic coupling in turbulent flows. *Annu. Rev. Fluid Mech.* **49**, 51–70.

HEISEL, M., HONG, J. & GUALA, M. 2018 The spectral signature of wind turbine wake meandering: a wind tunnel and field-scale study. *Wind Energy* **21** (9), 715–731.

HÖGSTRÖM, U., ASIMAKOPOULOS, D.N., KAMBEZIDIS, H., HELMIS, C.G. & SMEDMAN, A. 1988 A field study of the wake behind a 2 MW wind turbine. *Atmos. Environ.* **22** (4), 803–820.

HONG, J., TOLOUI, M., CHAMORRO, L.P., GUALA, M., HOWARD, K., RILEY, S., TUCKER, J. & SOTIROPOULOS, F. 2014 Natural snowfall reveals large-scale flow structures in the wake of a 2.5-MW wind turbine. *Nat. Commun.* **5**, 4216.

HOWLAND, M.F., BOSSUYT, J., MARTÍNEZ-TOSSAS, L.A., MEYERS, J. & MENEVEAU, C. 2016 Wake structure in actuator disk models of wind turbines in yaw under uniform inflow conditions. *J. Renew. Sustain. Energy* **8** (4), 043301.

HOWLAND, M.F., *et al.* 2020 Influence of atmospheric conditions on the power production of utility-scale wind turbines in yaw misalignment. *J. Renew. Sustain. Energy* **12**, 063307.

HOYT, J. & SEILER, P. 2020 Wind farm wake-steering exploration during grid curtailment. In *2020 American Control Conference (ACC)*, pp. 4052–4057. IEEE.

JIMÉNEZ, Á., CRESPO, A. & MIGOYA, E. 2010 Application of a LES technique to characterize the wake deflection of a wind turbine in yaw. *Wind Energy* **13** (6), 559–572.

KNOLL, D.A. & KEYES, D.E. 2004 Jacobian-free Newton–Krylov methods: a survey of approaches and applications. *J. Comput. Phys.* **193** (2), 357–397.

KROGSTAD, P.-Å. & ADARAMOLA, M.S. 2012 Performance and near wake measurements of a model horizontal axis wind turbine. *Wind Energy* **15** (5), 743–756.

LARSEN, G.C., *et al.* 2007 *Dynamic wake meandering modeling*. Risø National Laboratory.

LARSEN, G.C., MADSEN, H.A., THOMSEN, K. & LARSEN, T.J. 2008 Wake meandering: a pragmatic approach. *Wind Energy* **11** (4), 377–395.

LIEW, J.Y., URBÁN, A.M. & ANDERSEN, S.J. 2020 Analytical model for the power–yaw sensitivity of wind turbines operating in full wake. *Wind Energy Sci.* **5** (1), 427–437.

LIU, H., WANG, G. & ZHENG, X. 2019 Three-dimensional representation of large-scale structures based on observations in atmospheric surface layers. *J. Geophys. Res.* **124** (20), 10753–10771.

LOVRIC, M. 2011 *International Encyclopedia of Statistical Science*. Springer.

MÉCHALI, M., BARTHELMIE, R., FRANDSEN, S., JENSEN, L. & RÉTHORÉ, P.-E. 2006 Wake effects at Horns Rev and their influence on energy production. In *European Wind Energy Conference and Exhibition*, vol. 1, pp. 10–20. Citeseer.

MEDICI, D. & ALFREDSSON, P.H. 2006 Measurements on a wind turbine wake: 3D effects and bluff body vortex shedding. *Wind Energy* **9** (3), 219–236.

MENEVEAU, C. 2019 Big wind power: seven questions for turbulence research. *J. Turbul.* **20** (1), 2–20.

MUNTERS, W. & MEYERS, J. 2018 Dynamic strategies for yaw and induction control of wind farms based on large-eddy simulation and optimization. *Energies* **11** (1), 177.

NIAYIFAR, A. & PORTÉ-AGEL, F. 2016 Analytical modeling of wind farms: a new approach for power prediction. *Energies* **9** (9), 741.

OSSMANN, D., THEIS, J. & SEILER, P. 2017 Load reduction on a Clipper Liberty wind turbine with linear parameter-varying individual blade pitch control. *Wind Energy* **20** (10), 1771–1786.

PORTÉ-AGEL, F., BASTANKHAH, M. & SHAMSODDIN, S. 2020 Wind-turbine and wind-farm flows: a review. *Boundary-Layer Meteorol.* **174** (1), 1–59.

QIAN, G.-W. & ISHIHARA, T. 2018 A new analytical wake model for yawed wind turbines. *Energies* **11** (3), 665.

SAAD, Y. 1993 A flexible inner-outer preconditioned GMRES algorithm. *SIAM J. Sci. Comput.* **14** (2), 461–469.

SCHOTTLER, J., BARTL, J., MÜHLE, F., SÆTRAN, L., PEINKE, J. & HÖLLING, M. 2018 Wind tunnel experiments on wind turbine wakes in yaw: redefining the wake width. *Wind Energy Sci.* **3** (1), 257–273.

SHAPIRO, C.R., GAYME, D.F. & MENEVEAU, C. 2018 Modelling yawed wind turbine wakes: a lifting line approach. *J. Fluid Mech.* **841**, R1.

SHEN, W.Z., MIKKELSEN, R., SØRENSEN, J.N. & BAK, C. 2005 Tip loss corrections for wind turbine computations. *Wind Energy* **8** (4), 457–475.

SHEN, W.Z., ZHANG, J.H. & SORENSEN, J.N. 2009 The actuator surface model: a new Navier–Stokes based model for rotor computations. *Trans. ASME: J. Solar Energy Engng* **131** (1), 011002.

SMAGORINSKY, J. 1963 General circulation experiments with the primitive equations: I. The basic experiment. *Mon. Weath. Rev.* **91** (3), 99–164.

SORENSEN, J.N. & SHEN, W.Z. 2002 Numerical modeling of wind turbine wakes. *Trans. ASME: J. Fluids Engng* **124** (2), 393–399.

STEVENS, R.J.A.M. & MENEVEAU, C. 2017 Flow structure and turbulence in wind farms. *Annu. Rev. Fluid Mech.* **49**, 311–339.

THOMSEN, K. & SØRENSEN, P. 1999 Fatigue loads for wind turbines operating in wakes. *J. Wind Engng Ind. Aerodyn.* **80** (1), 121–136.

VEERS, P., DYKES, K., LANTZ, E., BARTH, S., BOTTASSO, C.L., CARLSON, O., CLIFTON, A., GREEN, J., GREEN, P. & HOLTTINEN, H. 2019 Grand challenges in the science of wind energy. *Science* **366** (6464), eaau2027.

WANG, G. & ZHENG, X. 2016 Very large scale motions in the atmospheric surface layer: a field investigation. *J. Fluid Mech.* **802**, 464–489.

WU, Y.-T. & PORTÉ-AGEL, F. 2012 Atmospheric turbulence effects on wind-turbine wakes: an LES study. *Energies* **5** (12), 5340–5362.

XIE, S. & ARCHER, C. 2015 Self-similarity and turbulence characteristics of wind turbine wakes via large-eddy simulation. *Wind Energy* **18** (10), 1815–1838.

YANG, X. 2020 Towards the development of a wake meandering model based on neural networks. In *Journal of Physics: Conference Series*, vol. 1618, p. 062026. IOP Publishing.

YANG, X., HOWARD, K.B., GUALA, M. & SOTIROPOULOS, F. 2015*a* Effects of a three-dimensional hill on the wake characteristics of a model wind turbine. *Phys. Fluids* **27** (2), 025103.

YANG, X., MILLIREN, C., KISTNER, M., HOGG, C., MARR, J., SHEN, L. & SOTIROPOULOS, F. 2021 High-fidelity simulations and field measurements for characterizing wind fields in a utility-scale wind farm. *Appl. Energy* **281**, 116115.

YANG, X., PAKULA, M. & SOTIROPOULOS, F. 2018 Large-eddy simulation of a utility-scale wind farm in complex terrain. *Appl. Energy* **229**, 767–777.

YANG, X. & SOTIROPOULOS, F. 2018 A new class of actuator surface models for wind turbines. *Wind Energy* **21** (5), 285–302.

YANG, X. & SOTIROPOULOS, F. 2019*a* A review on the meandering of wind turbine wakes. *Energies* **12** (24), 4725.

YANG, X. & SOTIROPOULOS, F. 2019*b* Wake characteristics of a utility-scale wind turbine under coherent inflow structures and different operating conditions. *Phys. Rev. Fluids* **4** (2), 024604.

YANG, X., SOTIROPOULOS, F., CONZEMIUS, R.J., WACHTLER, J.N. & STRONG, M.B. 2015*b* Large-eddy simulation of turbulent flow past wind turbines/farms: the virtual wind simulator (VWiS). *Wind Energy* **18** (12), 2025–2045.

YANG, X., ZHANG, X., LI, Z. & HE, G.-W. 2009 A smoothing technique for discrete delta functions with application to immersed boundary method in moving boundary simulations. *J. Comput. Phys.* **228** (20), 7821–7836.

ZHANG, W., MARKFORT, C.D. & PORTÉ-AGEL, F. 2013 Wind-turbine wakes in a convective boundary layer: a wind-tunnel study. *Boundary-Layer Meteorol.* **146**, 19.